Nagoya Institute of Technology

Low Temperature Growth of Graphene Using Low Melting Point Metals

低融点金属を用いたグラフェンの低温合成

By

Mona Ibrahim Araby

Thesis submitted for the award of the Doctoral (PhD) Degree of

Engineering

Department of Physicals Science and Engineering

Graduate School of Engineering

Nagoya Institute of Technology

Nagoya

Supervisor: Prof. Dr. Masaki Tanemura

September 2019

Dedicated to my beloved mother and father, teachers, friends and husband!

Declaration

I confirm that the work presented in this thesis is my own. Where I have consulted the work of others, it has been clearly stat

Contents

CHAPTER 2

EXPERIMENTAL METHODS AND CHARACTERIZATIONS

CHAPTER 3

CHAPTER 4

CHAPTER 5

CHAPTER 6

Acknowledgments

Alhamdulillah,

Up to this moment that putting my hands to type acknowledgments for thesis, I can't believe how fast time goes by. I am so grateful that God allowed me to go through that because it's made me. In this short page, I want to gratitude all surrounding me. This thesis would not have been possible without the help of many people.

I would first like to thank my supervisor **Prof. Dr.** Masaki Tanemura for his help, supporting, guidance and valuable advice in supervising my doctoral researches. I also want to thank **Prof. Dr.** Golap Kalita for the kind support, and **Prof. Dr.** Tetsuo Soga for his careful reading of this thesis.

I would especially like to thank **Dr.** Mohamed Saufi Rosmi, **Dr.** Subash Sharma, **Dr.** Kamal Sharma, **Dr.** Ritesh Vishwakarma for their assists and cooperation towards completing my research studies.

I am also thankful to my colleagues **Mr.** Balaram puddled and **Ms.** Sahar Elnobi Ibrahim for their cooperation, support, and encouragement. I would especially thankful to all masters and bachelor students of my lab for their help. They were always there to support me with motivations and advice and make my student life become a cheerful and enjoyable moments.

A special thanks to my beloved husband to keep supporting me until the end of my Ph.D. and my parent's words cannot express how grateful I am to all of you.

Abstract

Most of the researcher synthesized graphene using conventional methods, however, these methods have some disadvantages such as high-temperature synthesis process with the transfer process which is indispensable. For a wider range of practical applications synthesis graphene at a lower temperature is quite important wherefore, the recent research is focusing on synthesis graphene at low temperature, so in this dissertation, I challenged the synthesis of low-temperature graphene growth by using low melting points metals. ***In this work,*** I have successfully demonstrated that the melting point of the catalyst metal plays an important role to achieve the low-temperature growth of graphene, based on the high-resolution transmission electron microscopy (TEM) observation of the graphitization process. In order to achieve the low-temperature graphene growth, two strategies were attempted for the selection of the catalyst; one is using the low melting point metal as the catalyst and another is using the nano-sized particles to lower the melting point of the metal.

Chapter1, the introduction part about the history of graphene and unique properties and potential applications. The motivation and purpose of the thesis are also included in this chapter.

Chapter 2, discusses the experimental methods and the detailed characterizations process used in the present work.

Chapter 3, encouraged by the previous success in the graphene growth at 250^{o}C using a novel catalyst, Sn, in our group, indium (In) whose melting point is much lower than Sn was attempted as the catalyst here. In order to observe the local graphitization by TEM, In-included carbon nanofibers (In-CNFs) were fabricated on an edge of a carbon foil by Ar^{+} ion sputtering of both the carbon foil and an In plate. Depending on the ion energy, graphitization catalyzed by In was observed even for the as-sputtered sample without post-annealing, suggesting that In

is promising as the catalyst for the low-temperature graphene growth. Based on this fact, a stacked film of In and amorphous C was deposited onto a SiO_2 covered Si substrate, and this thin film sample was then annealed in vacuum at 150 and 200°C. In both cases, a clear 2D peak in Raman spectra, which is the evidence of the graphene formation, was observed.

Chapter 4, in order to check the temperature dependence of catalytic activity in local graphitization, CNFs including Sn nanoparticles (Sn-CNFs) were prepared on an edge of a carbon foil by Ar^+ ion sputtering of both the carbon foil and a Sn plate, and the Sn-CNFs were annealed in vacuum at 180 and 250°C. The Sn-CNFs was characterized by the dispersion of Sn nanoparticles 2-4 nm in diameter in amorphous CNFs. TEM observation revealed that the local graphitization started to occur at an annealing temperature of 180°C, which is much lower than the graphitization temperature for bulky Sn. The decrease in the melting point for the nano-sized particles was thought to be responsible for the local graphitization at a lower temperature.

Chapter 5, for the detailed observation of the graphitization process on insulator substrates by TEM, especially by cross-sectional TEM (X-TEM), the substrate thin enough to transmit the incidence electron should be developed. Here the fabrication of Si oxide nanofiber (SON) formed on a tip of an atomic force microscope (AFM) cantilever was also challenged for the future X-TEM observation of catalyst/graphene/substrate interface. Si-included CNFs (Si-CNFs) were fabricated onto AFM cantilever tips. The prepared Si-CNFs were then annealed at 1000°C in atmospheric ambient to form SON tipped cantilevers. SON, consisting of mostly Si and O, was linear in shape and was amorphous in the crystalline structure. The high performance of the SON tipped cantilever was demonstrated for the X-TEM analyses of ZnO films deposited thereon as a test sample, suggesting that it is promising as a substrate for X-TEM analyses.

Chapter 6, summarizes this work and explores future prospects.

List of Figures

Chapter 1. Introduction

1.1. History of Carbon Materials

Representing about 45-50% of all dry biomass, Carbon is considered the fundamental component of all known life on Earth. Owing to its abundancy on Earth, complex molecules are made by bonding of carbon and other elements such as hydrogen, oxygen, nitrogen, phosphorus, and sulfur. It has been assumed that if life exists in other places in the universe, it will be definitely based on carbon. Recently, carbon materials have been developed to form a brand of the inorganic nonmetallic material, which occupies an important place in materials science. Owing to its valences, Carbon is capable of forming many allotropes. It worth to mention that, carbon materials were used long time ago as an energy resources in form of coal and charcoal, which is composed by mixture crystallite structures of carbon known as amorphous carbon.

Large quantity of graphite was exposed in England In the 15th century, which was highly pure crystal. Graphite, which is one of the oldest allotropes soft materials, has been used as the brake linings, lead of pencils, and electrodes. Also, graphite-based materials can be used to produce carbon fibers, which have amazingly good mechanical properties enabling them to be suitable for aeronautic products and sports equipment [2]. In addition, graphite has revolutionized the world by the devilment of pencils (seen in **Fig. 1.1**). It worth to mention that diamond and graphite, since the late of the 18th century, were the most common allotropes of carbon materials, which exist in nature. After that, rapid progress in the development of carbon materials was achieved enabling them to take part in the industrial revolution.

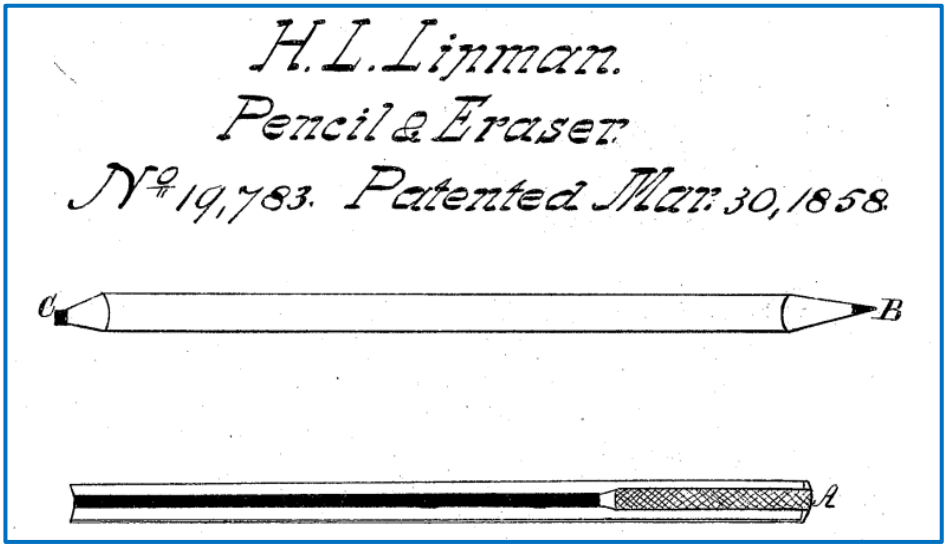

Figure 1.1: Hymen Lipman's pencil drawing in patent, which published in 1858 [1]

A new class of nanomaterials known as (C60) buckyballs or fullerenes was discovered in 1985 by a British chemist H.W. Kroto and a US scientist R. E. Smalley [3]. Their new material has a nanoscale spherical structure as fullerenes. Owing to its unique structure in addition to its chemical and physical properties, fullerene has a significant effect on many research topics including chemistry, physics, and materials science. Also, it was proven to be an attractive prospect regarding potential applications. Then, in 1991, Iijima's group discovered the carbon nanotubes (CNTs), with a title of "Helical microtubules of graphitic carbon" in Nature. CNTs are made of rolled up carbon layers with a single dimensional structure [4, 5]. Depending on the number of walls, CNTs can be classified as single-walled CNTs (SWCNTs), doublewalled CNTs (DWCNTs), and multiwalled CNTs (MWCNTs). Moreover, according to rolling up angle ("chiral vector"), they are called armchair, zigzag, and chiral nanotubes. Actually, the discovery of CNTs has resulted in intense researches on carbon-based materials, because of the fact that they display prominent electrical and mechanical properties.

1.2. Introduction to Graphene

2D dimensional graphite structure named graphene, a single layer of carbon, in 2004 was isolated by Manchester group [6]. They simply set a flake of graphite on scotch tape, and repeatedly peel off until the thinnest flakes are found. Due to their remarkable and pioneering research work, the Nobel Prize in Physics 2010 was jointly awarded to Geim and Novoselov for "groundbreaking experiments regarding the two-dimensional material graphene". The name "graphene" combines the information of "graph" due to the graphite and "ene" due to the carbon-carbon double bonds [7]. **Fig. 1.2** shows graphene as a basic building block for all other sp^2 hybridized carbon allotropes. It is clear that (a) 2-dimensional graphene is a basic component of the others. For example, (b) 1-dimensioan CNTs can be formed by rolling up, (c) 0-dimensional fullerene is the form of wrapping up with 60 carbon atoms, and (d) 3-dimensional graphite is a crystal that stacked by graphene layer.

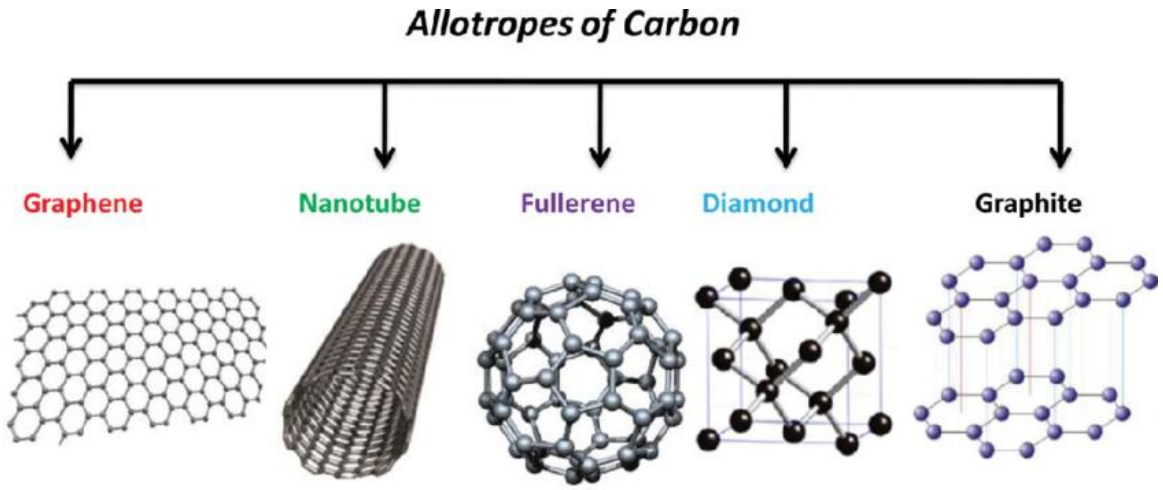

Figure 1.2: Various allotropes of carbon with geometrical transformations [8].

1.3. Structure and Properties of Graphene

1.3.1. Structure

The utilization of carbon materials for a huge number of applications gets from the materials' unique variety of structures and properties that provide from a chemical connection between carbon atoms to nanostructures, crystallite arrangement, and microstructures. Diamond and graphite are both three-dimensional (3D) crystalline forms of the element carbon. Graphite consists purely of sp^2 hybridized bonds, whereas diamond consists of sp^3 hybridized bonds. The carbon atoms in diamond are arranged in a lattice with face-centered cubic (fcc) crystal structure possessing excellent physical qualities, most of which originate from the strong covalent bonding between its atoms (sp^3 hybridization). For sp^2 hybridization, four valance electrons of C atom in 2s and 2p states excited together in the presence of an external perturbation (another atom) and one s-orbital and three p-orbitals (px, py, pz) being formed. One s-orbital and two p-orbitals contribute for the sp^2 hybridization resulting in planer assembly of graphene honeycomb structure with characteristic angle of 120^o between the hybridized orbitals (covalent σ-bonds). The remaining p-orbital perpendicular to hybridized network contributes for the week van der Waals interaction between graphene layers with so formed π-bond [**Fig. 1.2 (b)]** [9]. In 1947, P. R. Wallace used graphene as a simple theoretical model for the description of the 3D material and studied the band structure of graphite [10]. In each layer, the carbon atoms are organized in a hexagonal lattice with separation of 1.42 Å [**Fig. 1.2 (a)**], (sp^2 hybridization), and the distance between planes (layers) is 3.37 Å [10, 11].

The two known forms of graphite, α (hexagonal) and β (rhombohedral), have fundamentally same physical properties. Graphitic carbon nanomaterials can be individuals from the same group because they consist mostly of sp^2 carbon atoms organized in a hexagonal lattice. Wallace successfully identified graphene as a zero band gap semiconductor (semi-metal) and

with extraordinarily high mean free path within graphene sheet [12, 13]. The linear energy distribution around the Dirac point [**Fig. 1.2 (c)**] due to the 2D honeycomb structure of graphene (lattice constant 2.46Å) makes this material different than other semiconductors in property and hence paves the avenues range of application [8, 14].

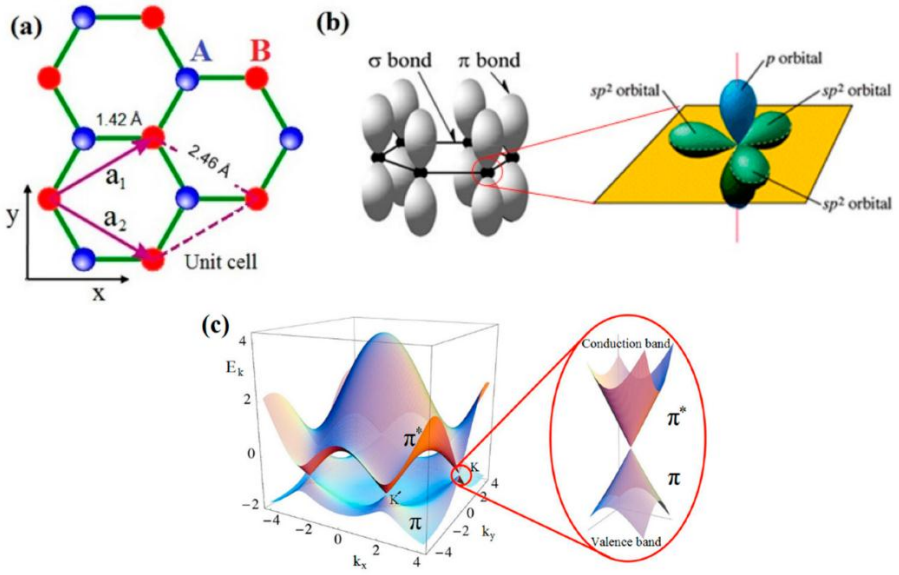

Figure 1.3: (a) Bravais lattice of graphene with lattice constant 2.46 Å. (b) π-bond σ-bonds configuration in a honeycomb. (c) Electronic dispersion in honeycomb lattice with zoom in of energy band close to Dirac point [12].

1.3.2. Properties of Graphene

1.3.2.1. Electronic Properties

One of the most useful properties of graphene is that it is a zero-overlap semimetal with very high electrical conductivity. Graphene is a zero-gap semiconductor because its conduction and valence bands meet at the Dirac points. At the Dirac point, the density of states is zero and the linear dispersion relation results in an effective mass of zero [15]. Therefore, graphene displays remarkable electron mobility at room temperature, with reported values in excess of 15000 $cm^2\ V^{-1}\ s^{-1}$ [16, 17].

1.3.2.2. Optical Properties

Graphene has very high transparency of about 97.7% of a single layer and has been experimentally observed in the visible range, which means that atomic monolayer graphene has a surprisingly high opacity, absorbing $\pi\alpha \approx 2.3\%$ of visible light [18]. This property makes graphene a suitable material for fabrication of transparent and flexible electrodes [19], touch screens [20], photodetectors [21] and solar cells [22].

1.3.2.3. Mechanical Properties

Graphene is one of the strongest materials ever tested with a tensile strength of 1.3×10^{11} Pa, it is harder than diamond and stronger (between 10 and 300 times) than steel. Young's modulus of graphene is a remarkably high ~ 1TPa with an ultimate tensile strength of 130GPa [23]. This robustness could be used to reinforce other materials [24] or to produce composite materials with graphene [25]. Having mechanical properties, improve strength in many composite materials.

1.3.2.4. Thermal Properties

The thermal conductivity of graphene at room temperature is about 5×10^3W/m K [26] which is 10 times higher than the thermal conductivity of copper (401 W/m K) [27]. Experimentally calculated thermal conductivity of graphene is in the range of 3000-5000 W/m.K and is strongly depends on the flake size and width of graphene sheet (the larger segment, more heat it could transfer) [28, 29]. This property can be used in micro-detectors for gas molecules, by monitoring the dramatic change in resistance induced by adsorption and desorption of gas molecules [30].

1.4. Potential applications of graphene:

The previously mentioned hugely fascinating and different properties displayed by graphene open up its application in regions spreading throughout all disciplines of science. **Fig. 1.4** represented some novel applications of graphene.

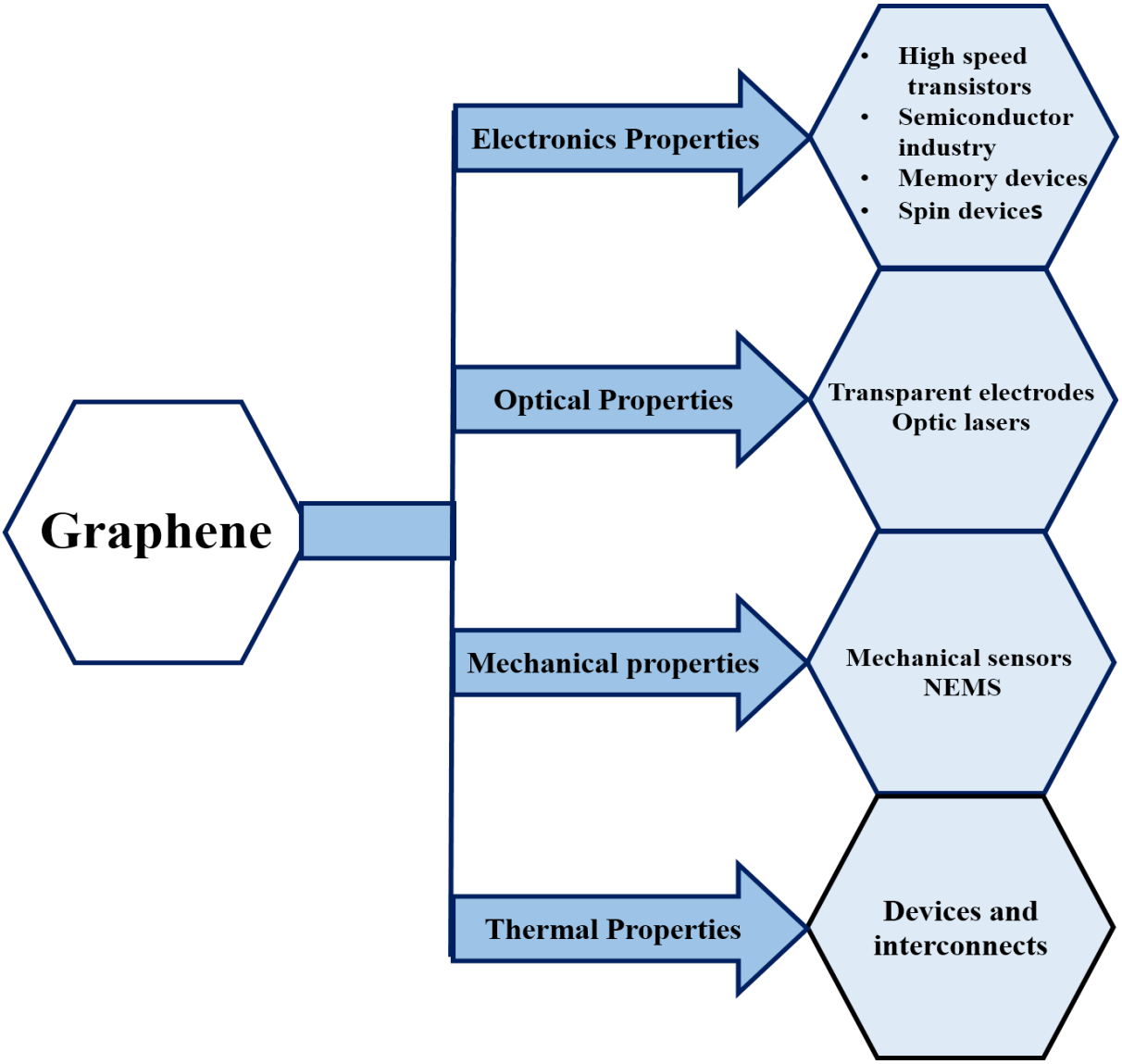

Figure 1.4: Some novel applications of graphene [31].

1.5. Synthesis techniques

Commonly used techniques for the fabrication of graphene are summarized in Table 1. 1.

Table 1. 1: Summary of common methods for the isolation or synthesis of graphene [32].

Technique	Brief Description	Product details	Advantage	Disadvantage
Micro Mechanical exfoliation	Graphene layers exfoliate by using sticky tape	Mono to few layered flakes size: (μm-cm)	Best for Fundamental research, High quality, simple and cheap.	Varied number of layers, small scale production, inconsistent
Liquid phase exfoliation (LPE)	Specialized solvent is utilized for the exfoliation of graphite by ultra-sonication	Mono to few-layer graphene flakes dispersed in liquid Size: up to μm	Easy and time efficient method, cheap and scalable, produced highly concentrated graphene oxide suspension	Uncontrollable size and layer number, significant defects, extraction from liquid essential
Reduction of graphene oxide (GO)	Chemically reduced the GO exfoliated solvent into graphene	Mono to few-layer graphene suspension Size: up to μm	Versatile technique for large area production can be stored in water	Hazardous chemical involved, only final product is stable in hydrophilic polymers
Thermal decomposition of SiC	High temperature employed to evaporate Si form SiC wafer	Mono to few-layer graphene films Size: up to cm	Epitaxial growth, low number of defects, control in thickness of film	Small scale producing, expensive, unscalable
Chemical Vapor Deposition (CVD)	Gaseous carbon source dehydrogenated into graphene on the metal surface at high temperature	Mono, bi and few-layer graphene Size: cm to m	Scalable method, a wide range of metals utilized as a substrate, large area up to few inch uniform film, various technique approaching monolayer film	Effort essential for the control of nucleation, High temperature, energy and time inefficient,

1.6. Challenge of direct growth of graphene at low temperature for future device applications

The development of two-dimensional graphene layers has recently attracted considerable attention because of its extraordinary electrical, mechanical and chemical properties of graphene make it suitable for various applications such as being used as interconnections for nanoelectronics devices, and next generation semi-conductor and energy storage devices. It is worth mentioning that most of the reported graphene syntheses include a high-temperature process. CVD, which is one of the most popular methods for graphene synthesis, can synthesize high-quality graphene only at high temperatures (usually higher than1000^{o}C) on metal catalyst foils. In addition, for device applications, CVD grown graphene should be transferred onto the desired substrate. During transfer of CVD grown graphene, a metal substrate is chemically etched followed by tedious and time-consuming cycles of cleaning. However, for a wider range of practical applications, low-temperature growth should be achieved. Thus, much effort has been devoted to the low-temperature graphene growth. In this regard, material scientists and researchers have mainly focused on two typical problems: **i)** direct growth and **ii)** low-temperature growth of graphene.

1.6.1. Direct Growth on Suitable Substrates

To avoid the issues related to graphene transfer, two different growth approaches, catalytic growth and non-catalytic growth, have been used for the growth of graphene monolayers directly on the desired substrates [33-35]. Graphene monolayers have been grown successfully on flexible and rigid substrates using catalytic and non-catalytic growth processes [36, 37]. Synthesis of graphene has been also demonstrated by metal-assisted crystallization of a thin C film at an elevated temperature. In the metal-assisted crystallization

process, C atoms diffuse through the metal layer at a high temperature to form graphene at the top of the surface and at the interface between catalyst metal and the substrate. For example, by using the catalyst of Co with Co oxide on top, few-layer graphene has been synthesized directly on the SiO_2 substrate by the simple vacuum annealing at 800^oC for a Co-oxide/Co/amorphous C/SiO_2 multi-stacking film system [38]. If the growth temperature can be reduced by using novel catalysts, it will be fascinating, though it is quite challenging.

1.6.2. Low-temperature Growth

Most of the reported graphene synthesis includes the high-temperature process [39, 40]. CVD, which is one of the most popular methods for the graphene synthesis, can synthesize high-quality graphene only at high temperatures (usually higher than 1000^oC) on metal catalyst foils. For a wider range of practical applications, and also from a view point of energy saving, lower temperature growth is still major challenges in the graphene research. For example, Marchena et al. have achieved direct graphene growth on a flexible glass at 700^oC [41]. Sulaiman et al. and Jang et al. demonstrated the CVD graphene growth on Cu at 450 and 300^oC by using chlorobenzene and benzene, respectively, as a carbon source [42, 43].

Very recently, the low-temperature graphene growth using novel catalysts, which have been rarely used for the conventional CVD, were successfully attempted. Fujita et al. [44] and Park et al. [45] employed Ga and Ti, respectively, to achieve the CVD graphene growth at the temperatures lower than 150^oC. In our group also, we demonstrated the graphene growth just by the simple vacuum annealing of the stacked C and catalyst films on insulator substrates at 250 ^oC for Sn as novel catalysts [46]. So, the melting point seems to play an important role in low-temperature graphene growth. In order to understand the graphitization process for those low melting point metals, detailed observation of the catalyst behavior in (TEM) will

be important. In this thesis, I dealt with the newest findings on this interesting subject, leading to an additional strategy to achieve lower temperature graphene growth using low MP catalyst. MP and evaporation temperature strongly depend on the size of nanoparticles (NPs), and are lower than those for bulk materials, due to their relatively large surface area [47]. So, the low-temperature graphene formation would be due to the decreased melting point of the small size of NPs. **Fig.1.4** illustrate of the relation between the particle and the temperature[48]. In this thesis, graphene growth using NPs were also attempted.

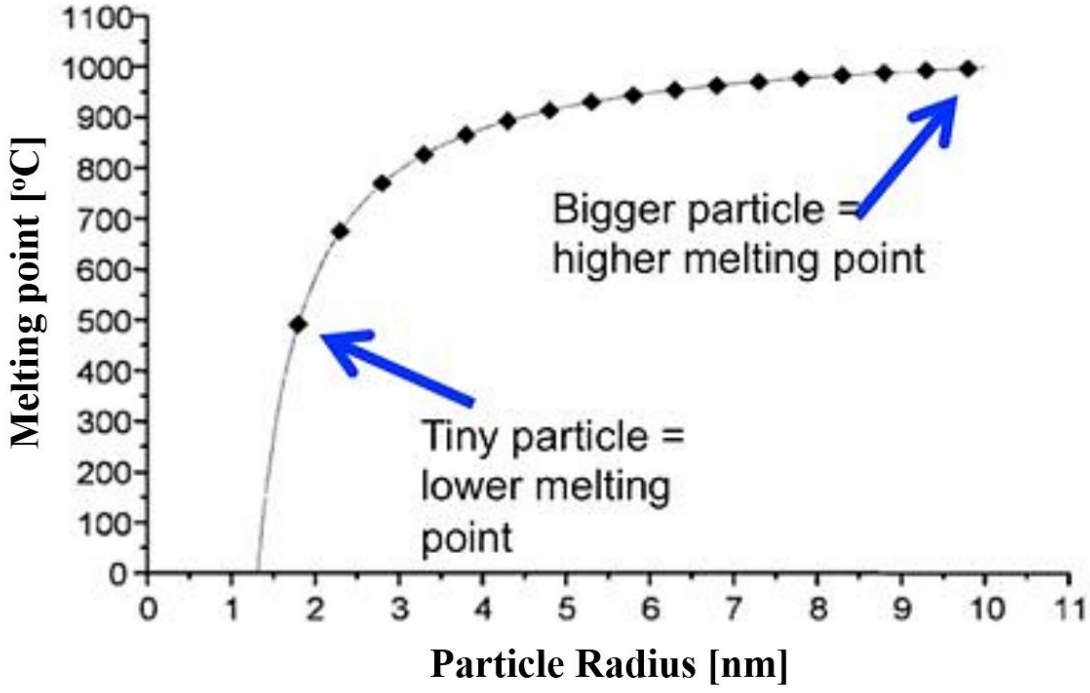

Figure 1.5: Relationship between particle size and melting point of gold nanoparticles [48].

1.6.3. Motivations and Purposes of the Thesis

As described above, for a wider range of practical applications, the transfer-free graphene growth at lower temperatures is still the main challenge in the graphene research. And the previous work in our group on the low-temperature graphene growth using a novel catalyst, Sn, strongly inspired me to explore further catalysts to achieve this goal.

In CVD process, for example, a well-known Cu catalyst case, adsorption, and decomposition of carbon contained molecules and recrystallization of carbon atoms (graphitization) occur at about 1000^{o}C which is very close to the melting point of Cu. This seems to suggest that the melting point of the catalyst metal plays an important role in the graphitization. If so, what will happen for the low-temperature metals as a catalyst? As expected, Sn surely acts as a catalyst. What about other low melting point metals? Is the low melting point metal generally usable for the low-temperature growth of graphene? Another strategy to lower the melting point is to use the nano-sized catalysts. In general, melting point decreases with a decrease in the particle size in nanometer range. If the nanoparticles are used as catalyst, is the further reduction in the graphene growth temperature achievable? This thesis was designed to answer those questions. To answer those questions, I focused on the fundamentals obtained by transmission electron microscopy (TEM). For the TEM analyses, especially for the cross-sectional TEM analyses, the sample preparation is very time-consuming and generally difficult. In order to provide a platform usable as a simple substrate for the cross-sectional TEM, Si oxide nanofiber grown on a Si cantilever originally used for atomic force microscope was also proposed in this thesis.

1.7. References

[1] H. Lipman, Combination of lead-pencil and eraser U.S. Patent **30**, 19783, 1858.

[2] E. Fitzer, A. Gkogkidis, M. Heine, High Temperatures-High Pressures, **16**, 363-392, 1984.

[3] H. W. Kroto, J. R. Heath, C. O'brien, R. F. Curl, and R. E. Smalley, Nature **318**, 162, 1985.

[4] S. Iijima, Nature **354**, 56, 1991.

[5] W. A. de Heer, A. Chatelain, D. Ugarte, Science **270**, 1179, 1995.

[6] K. S. Novoselov, A. K. Geim, S. V. Morozov, D. Jiang, Y. Zhang, S. V. Dubonos, V. Grigorieva, and A. A. Firsov, Science **306**, 666, 2004.

[7] H. P. Boehm, R. Setton, E. Stumpp, Applied Chemical **66**, 1893, 1994.

[8] A. K.Geim, K. S. Novoselov, Natural Material **6**, 183, 2007.

[9] L., Gao, G.-X., Ni, B. Liu, A. H., Castro Neto, K. P., Loh. Nature, **505**, 190, 2014.

[10] P. R.Wallace, Physical Review **71**, 622,1947.

[11] G. S. Painter, D. E. Ellis, Physical Review B 1, 4747, 1970.

[12] L.Gao, GX2. Ni, B. Liu, A. H.Castro Neto, K. P Loh, Nature **505**, 190, 2014.

[13] J.W. McClure, Physical Review, **108**, 612, 1957.

[14] K. S.Novoselov, A. K. Geim, S. V. Morozov, D.Jiang, M. I.Katsnelson, I. V.Grigorieva, S. V. Dubonos, A. A. Firsov, Nature **438**, 197, 2005.

[15] K. F. Mak, C. Lee, J. Hone, J. Shan, T. F. Heinz, Physical Review Letter **105**, 136805, 2010.

[16] K. I.Bolotin, K. J. Sikes, Z. Jiang, M. Klima, G. Fudenberg, J. Hone, P. Kim, H. L. Stormer, Solid State Communications **146**, 351, 2008.

[17] X. Du, I. Skachko, A. Barker, E. Y. Andrei, Nature Nanotechnology **3**, 491, 2008.

[18] R. R. Nair, P. Blake, A. N. Grigorenko, K. S. Novoselov, T. J. Booth, T. Stauber, N. M. R. Peres, A. K. Geim, Science **320**, 1308, 2008.

[19] K. S. Kim, Y. Zhao, H. Jang, S. Y. Lee, J. M. Kim, K. S. Kim, J.-H. Ahn, P. Kim, J.-Y. Choi, B. H. Hong, Nature **457**, 706, 2009.

[20] S. Bae, H. Kim, Y. Lee, X. Xu, J. S. Park, Y. Zheng, J. Balakrishnan, T. Lei, H. R. Kim,Y. I. Song, Y.-J. Kim, K. S. Kim, B. Ozyilmaz, J. H. Ahn, B. H. Hong, S. Iijima, Nature Nanotechnology **5**, 574, 2010.

[21] X. Wang, L. Zhi, K. Müllen, Nano Letters **8**, 323, 2008.

[22] F. Xia, T. Mueller, Y.-m. Lin, A.Valdes-Garcia, P. Avouris, Nature Nanotechnology **4**, 839, 2009.

[23] C. Lee, X. Wei, J. W. Kysar, J. Hone, Science, **321**, 395, 2008.

[24] C. L. P. Pavithra, B. V. Sarada, V. Rajulapati Koteswararao, T. N. ABD Rao, G. Sun-Dararajan, Sci. Rep. **4**, 4049, 2014.

[25] Q. Wang, C. Wang, M. Zhang, M. Jian, Y. Zhang, Nano Letters **16**, 6695, 2016.

[26] D. C. Elias, R. R. Nair, T. M. G. Mohiuddin, S. V. Morozov, P. Blake, M. P. Halsall, A. C. Ferrari, D. W. Boukhvalov, M. I. Katsnelson, A. K. Geim, K. S. Novoselov, Science **323**, 610, 2009.

[27] K. Saito, J. Nakamura, A. Natori, Phys. Rev. B. Phys **76**, 115409, 2007.

[28] D. L. Nika, S. Ghosh, E. P. Pokatilov, A. A. Balandin, Appl. Phys. Lett. **94**, 203103, 2009.

[29] A. A. Balandin, S. Ghosh, W. Bao, I. Calizo, D. Teweldebrhan, F. Miao, C. N. Lau, Nano Lett. **8**, 902, 2008.

[30] C. Berger, Z. Song, X. Li, X. Wu, N. Brown, C. Naud, D. Mayou, T. Li, J. Hass, A. N. Marchenkov, E. H. Conrad, P. N. First, W. A. de Heer, Science **312**, 1191, 2006.

[31] M.E. Ayhan, Synthesis of Graphene by Chemical Vapor Deposition and Solid Phase Reaction Process (Doctoral dissertation), 2014.

[32] K. P.Sharma, Synthesis and characterization of graphene and hexagonal BN crystals on Cu by chemical vapor deposition using solid precursors (Doctoral dissertation), 2018.

[33] M. H. Rummeli, A. Bachmatiuk, A. Scott, F. Borrnert, J. H. Warner, V. Hoffman, J.-H. Lin, G. Cuniberti, and B. Buchner ACS Nano. **4**, 4206, 2010.

[34] J. Chen, Y. Wen, Y. Guo, B. Wu, L. Huang, Y. Xue, D. Geng, D. Wang, G. Yu, and Y. Liu, J. Am, Chem. Soc.**133**, 17548, 2011.

[35] L. Zhang, Z. Shi, Y. Wang, R. Yang, D. Shi, and G. Zhang, Nano Res. **4**, 315-21, 2011.

[36] R. Steingrüber, M. Ferstl, and W. Pilz, Microelectron. Eng. **57**, 285, 2001.

[37] J.-H. Lee, M.-S. Kim, J.-Y. Lim, S.-H. Jung, S.-G. Kang, H.-J. Shin, J.-Y. Choi, S.-W. Hwang, and D. Whang, Appl. Phys. Lett. **109**, 053102, 2016.

[38] Ryo Hirano, Ken Matsubara, Golap Kalita, Yasuhiko Hayashia and Masaki Tanemura, Nanoscale, **4**, 7791, 2012.

[39] X. Li, W. Cai, J. An, S. Kim, J. Nah, D. Yang, R. Piner, A. Velamakanni, I. Jung, E. Tutuc, S. K. Banerjee, L. Colombo, and R. S. Ruoff, Science, **324**, 1312, 2009.

[40] A. Reina, X. Jia, J. Ho, D. Nezich, H. Son, V. Bulovic, M. S. Dresselhaus and K. Jing, Nano Lett. **9**, 30, 2009.

[41] M. Marchena, D. Janner, T. L. Chen, V. Finazzi and V. Pruneri, Opt. Mat. Express, **6**, 3324, 2016.

[42] K. Sulaiman, A. Y. Ali, D. Elkington, K. Feron, K. F. Anderson, W. Belcher, P. Dastoor and X. Zhou, Carbon **107**, 325, 2016.

[43] J. Jang, M. Son, S. Chung, K. Kim, C. Cho, B. H. Lee, and M. Ham, Sci. Rep. **5**, 17955, 2015.

[44] J. Fujita, T.Hiyama, A. Hirukawa, T.Kondo, J.Nakamura, S. Ito, R.Araki, Y. Ito, M. Takeguchi and W.Pai, Sci. Rep., **7**, 12371, 2017.

[45] B.Park, J.S. Choi, J. H. Eom, H. Ha, H. Y. Kim, Se.Lee, H. Shin, and .G. Yoon, ACS Nano.**12**, 2016, 2018.

[46] R. Vishwakarma, M.S. Rosmi, K. Takahashi, Y. Wakamatsu, Y. Yaakob, M. I. Araby, M. Kitazawa, M. Tanemura, Sci. Rep. **7**, 43756, 2017.

[47] D. Guo, G. Xie, J. Luo, J. Phys. D. Appl. Phys. **47**, 13001, 2014.

[48] G. Schmid, B. Corain, J. Inorg. Chem. **17**, 3081-3098, 2003.

Chapter 2. Experimental Methods and Characterizations

2.1. Experimental Methods

In this section 2.1, the detailed explanation for the synthesis of metal incorporated CNFs and atomic force microscopy (AFM) cantilevers sometimes used as the substrate for the CNF growth are described.

2.1.1. Ion Irradiation method

The samples of carbon nanofibers (CNFs) for this study were fabricated by ion irradiation of carbon base substrate. The substrate was sputtered with Ar^+ ions, using a Kaufman-type ion gun (Ion Tech. 3-1500-100FC). The sample fabrication was carried out at an ion incident angle of 45° from the surface normal since an oblique Ar^+ ion bombardment is known to be suitable for the ion-induced CNF synthesis [1]. The ion beam employed was 6 cm in diameter. Ion irradiations at 600 eV and, 1000 eV were performed for 1 hr at room temperature. The basal and working pressures for the fabrication of the ion-induced CNFs were 1.5×10^{-5} and 2×10^{-2} Pa, respectively. The system was evacuated by a rotary pump and a turbo molecular pump.

Commercially available carbon foil with a thickness of 100 μm was mainly used for the sample fabrication. For the fabrication of the composite ion-induced CNFs, the substrate C foil was placed perpendicularly to the target material (in this thesis; In, and Sn) plate as a metal supply source, and was co-sputtered with Ar^+ ions [**Fig. 2.1**]. After the ion irradiation, the surface morphology and crystallinity of the samples were carefully observed by scanning electron microscopy (SEM) and transmission electron microscopy (TEM).

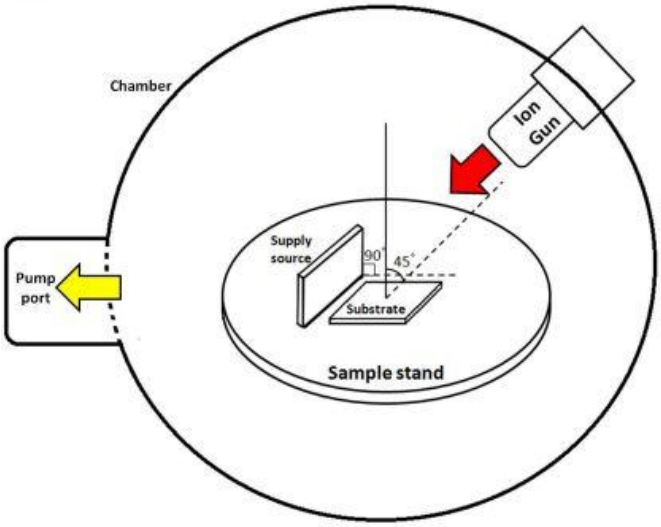

Figure 2.1: Schematic of an ion irradiation experimental setup

2.1.2. Formation of carbon nanofibers (CNFs)

A detailed mechanism of the ion-induced CNF growth is described elsewhere [2-5]. In brief, **(i)** re-deposition of carbon atoms sputter-ejected from the surface onto the sidewall of the conical protrusions, **(ii)** the surface diffusion of the re-deposited carbon atoms towards the tip of the respective cones during ion irradiation, and hence **(iii)** forming a CNF. Schematic diagram of the growth mechanism of ion-induced CNF is shown in **Fig. 2.2**. As described above, in this CNF growth, various kinds of metals and semiconductors can be supplied to fabricate composite CNFs.

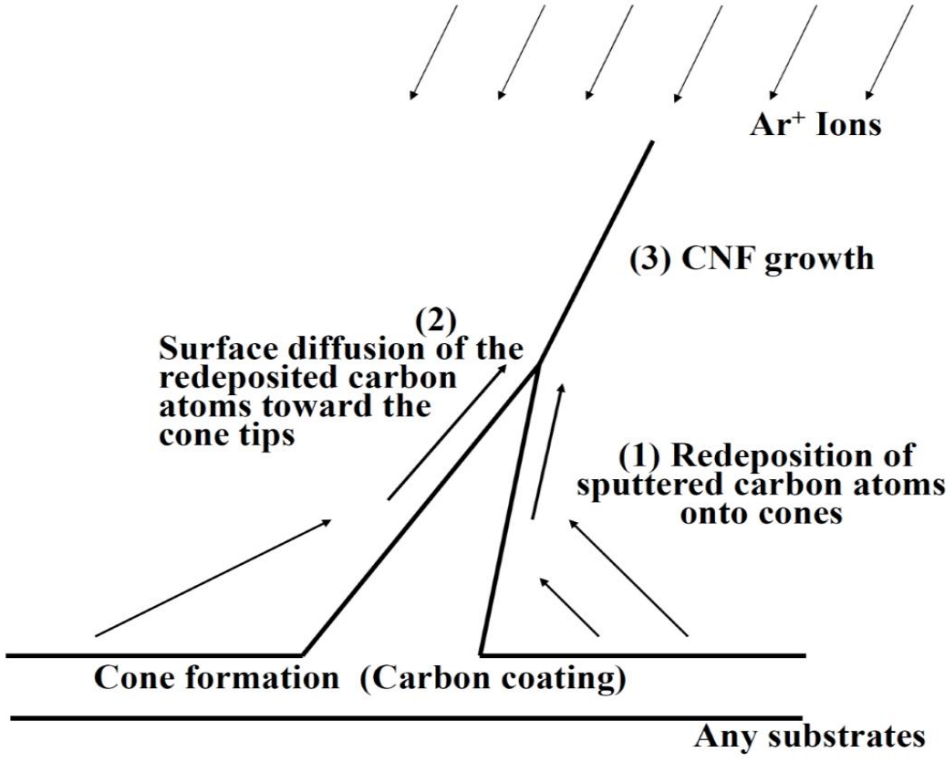

Figure 2.2: Schematic representation of the growth mechanism of ion-induced CNF. [5]

2.1.3. Atomic Force Microscopy (AFM) Cantilevers

Atomic force microscopy (AFM), which is a very-high-resolution type of scanning probe microscopy, is designed to measure the topography of a sample, with a demonstrated resolution in the order of nanometer. AFM analyses were carried out with a JSPM-5200 scanning probe microscope in tapping mode. The tip of the cantilever "touches" the sample which topographically gives information about the surface of the sample, in which the repulsion forces push the tip upward. The variations in height of the tip can be measured with a laser beam which reflects on the cantilever. A photodiode can then detect the movement of the beam and consequently the movement of the cantilever and tip. The movement is converted into a change in voltage. Then, an image of the surface can be seen as a reproduction of the variations in voltage. It can be used to see, for example, the step edge between graphene and a substrate and thus be able to calculate the thickness of graphene layers.

2.2. Characterizations

2.2.1. Scanning electron microscopy (SEM)

Scanning electron microscope (SEM) is a type of electron microscope that provides the details of surfaces information by scanning the surface with an electron beam [6]. Morphological analyses were carried out by Scanning electron microscopy (SEM) studies with (JEOL JSM 5600) scanning electron microscope. **Fig. 2.3** shows the schematic diagram of the technology of a SEM, this type of electron beam microscope the electron bean traces sample in a raster pattern. The signals that derive from electron surface interactions expose information about the surface with external morphology, crystal structure, chemical composition, and so on. In most applications, information are collected over a specific space of the surface of the sample, and a 2D image is generated that displays spatial variations in these properties. The beam is concentrated on the stage, where a sample is employed. For the CNFs case, images were taken up with a magnification range of 20X to about 30.000X and spatial resolution of 50 to l00 nm.

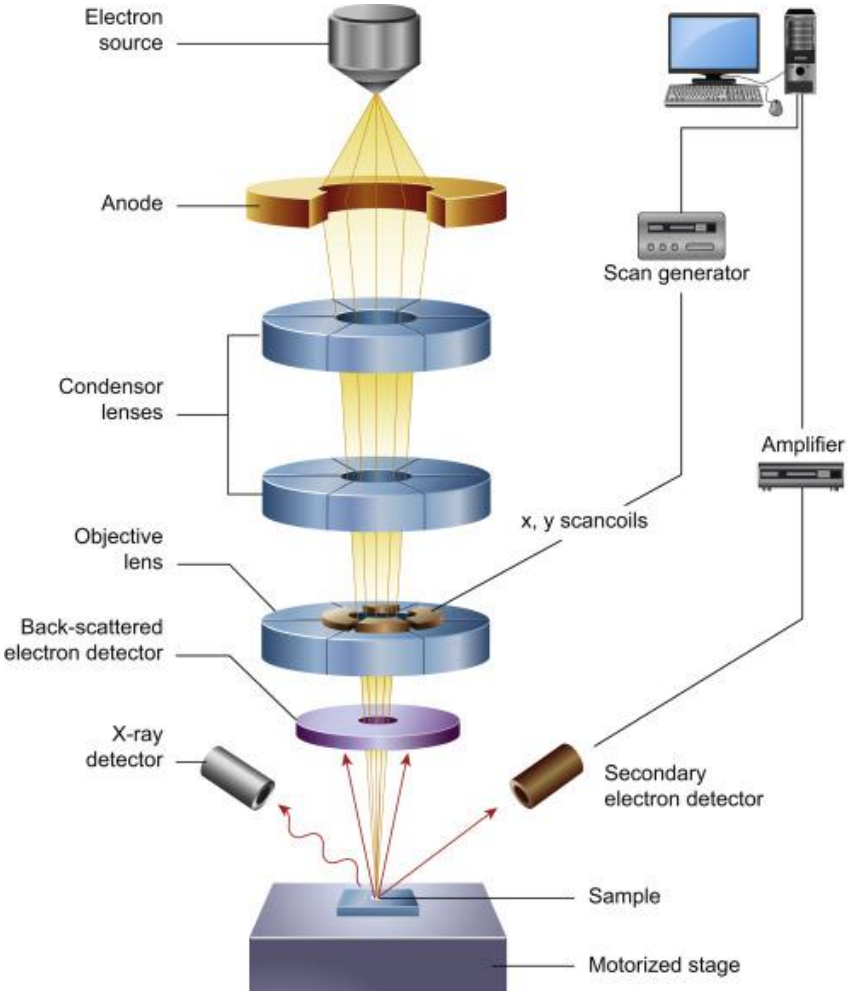

Figure 2.3: Schematic diagram of SEM [7]

2.2.2. Transmission Electron Microscopy (TEM)

Transmission electron microscope (TEM) is a very powerful instrument for material science to observe the features of very small specimens. A high energy beam of electrons is transmitted through an ultra-thin specimen to form an image. TEM can be used to characterize the morphology, crystal structure, and elemental information of membrane materials. The quality, shape, size, and density of quantum can be used to investigate by high-resolution of TEM. Due to the optical function TEM can be divided into three main parts: (1) the illumination part, (2) the objective lens system, (3) the imaging system [8]. TEM employs the electron gun which the shape is applied by electromagnetic lenses while the visible light shaped by glass lenses is

used as a source in an optical microscope. Furthermore, TEM demands high vacuum surrounding while optical microscope only needs surrounding pressure. The comparison of TEM and the optical microscope is summarized in **Table 2.1**.

Table 2.1. Comparison of TEM and optical microscope construction. [9]

	TEM	**Optical Microscope**
Illumination system	Electron gun	Visible light
Lenses	Electromagnetic lenses	Glass lenses
Surrounding	High vacuum	Atmosphere

A schematic diagram representing imaging and diffraction modes which are the main parts of the microscope is illustrated in **Fig. 2.4.** TEM usually consists of three stages of lensing. The stages contain the condenser lenses, the objective lenses, and the projector lenses. The first stage is The condenser lenses which is responsible for primary beam formation, second is the objective lenses which is focusing on the beam that comes through the sample, and the last stage is projector lenses which are used to expand the beam onto the phosphor screen.

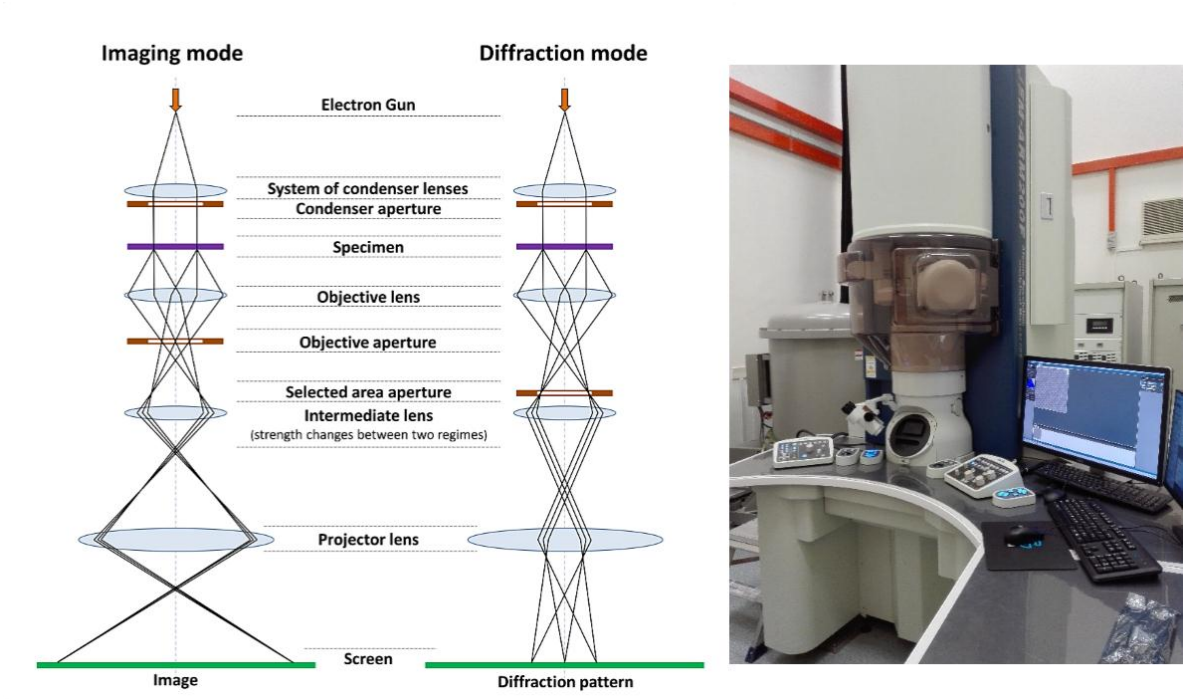

Figure 2.4: Schematic diagram showing the main parts of the basic TEM [10] and TEM model: JEM-ARM200F (JEOL) used in the thesis.

2.2.3. Microanalysis in TEM

In addition to its high-resolution imaging, TEM investigation has the ability to combine these imaging techniques with other generated signals in order to analyze the chemistry of the specimens. A microanalysis is a study to analyze specimens chemistry by using the Analytical Transmission Electron Microscope (ATEM). It worth to mention that most of the modern TEMs, which are operating at intermediate voltages of 200/300 keV, are equipped with functions to carry out (scanning) transmission electron microscopy ((S)TEM) along with energy dispersive X-ray spectroscopy (EDX) as well as the complementary techniques of electron energy loss spectroscopy (EELS). In all experiments performed in this thesis, EDX has been utilized for the microanalysis.

2.2.3.1. Energy-dispersive X-ray spectroscopy (EDX) Analysis

EDX is an analytical technique which is used for identifying and quantifying elemental compositions of a specimen. Accordingly to the ionized atoms inside the TEM specimen there is a possible transition within the internal shells of the atom which is associated with the emission of a characteristic X-ray. Special detectors are used to receive the emitted X-ray photons in order to generate the plot of X-ray counts versus X-ray energy. Conventional X-ray detectors, which are semiconductor-based such as lithium (Li) doped silicon (Si) are protected by an ultrathin window, which is cooled by liquid nitrogen in order to prevent the thermal noise during the collection.

2.2.4. Measurement setup in TEM

2.2.4.1. *In-situ* TEM

TEM is considered one of the most useful tools that can be used to realize a thorough understanding of sample structure and composition at the atomic level. Ex-situ experiments can only be used to investigate the state of the sample at the beginning and t the ending of experiment, whereas the phenomenon happening during the process remains unknown. As a result, there are many unanswered questions regarding the transformation, their kinetic and state of the materials. In addition, the changes in environment such as pressure and oxidation process can play an important role in the experiment.

On the other hand, Performing of *in-situ* TEM experiments to understand the dynamics of sample change under several external conditions like heating, cooling, interaction with the reactive environment, electrical biasing and, mechanical deformation, etc. in the real time. External stimulus and real-time observations are considered the main components of the *in-situ* experiments. However, special TEM holders are needed in order to put on different external

stimulus inside the TEM, which are the most crucial part. In addition, a fast recording system is essential for real-time observations.

2.2.4.2. Holders for *in-situ* TEM measurements

2.2.4.2.1 Electrical measurements

Obviously, **Fig. 2.5** shows a photograph of the e *in-situ* TEM holder (JEOL; EM-Z02154T) for current-voltage (I-V) measurement. The TEM (I-V) sample holder employs two stages, which are stationary and piezo-driven stages. As shown in **Fig. 2.6**, the main sample is mounted on the stationary stage of the I-V holder, whereas tungsten nanoprobe is placed on the piezo-driven stage. In order to control the piezo-driven stage in x, y and x directions, three direct currents (DC) power supplies are connected with the I-V TEM sample holder to derive the piezoelectric devices as shown in **Fig. 2.7**.

A two-channel (KEITLEY: 2400) and (Agilent B2912A) are also used in the I-V measurement system to connect the *in-situ* TEM holder. This accurate unit can supply a voltage with very small increment (in the range of millivolt) up to a maximum voltage of 250V, which is controlled by the I-V measurement computer software, as shown in **Fig. 2.8**. While applying voltage to the I-V measurement system, the current is accurately measured in order to investigate the changes in specimen structure. In this study, *in-situ* TEM facility is used to measure the I-V characteristics of a single CNF that has been carried out under the working pressure of 1×10^{-5} Pa. Also, the microscope was operated at an acceleration voltage of 200 kV. A Charge-coupled device (CCD) camera associated with an image recording application is used to continuously record TEM images. It worth to mention that during the I-V measurement, the sample structural behavior and transformation were also observed.

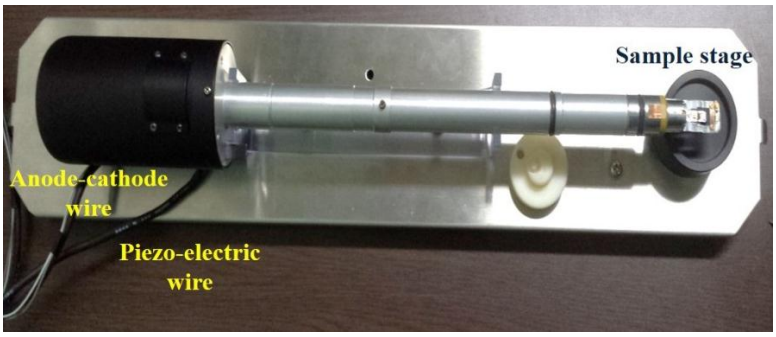

Figure 2.5: I-V TEM specimen holder.

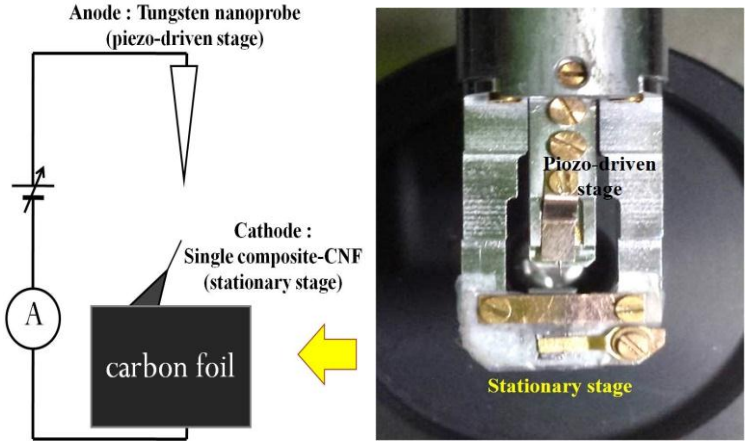

Figure 2.6: Sample setup on a TEM specimen holder.

Figure 2.7: 3 DC power supplies used for piezoelectric devices.

Figure 2.8: Electrical measurements setup.

2.2.4.2.2 Heating experiments

For numerous experiments, samples need to be heated *in situ* in the microscope. **Fig. 2.9** shows the model 652 double tilt heating holder which is a furnace type holder designed to authorize the direct observation of microstructural phase changes, nucleation, growth, and dissolution process at elevated temperatures. The furnace of the 652 double tilt holder is made of either tantalum or Inconel®. The furnace of the 652 double tilt holder is made of either tantalum or Inconel®. The tantalum furnace provides high-temperature strength and resistance to solid-state welding for most materials including silicon. Also, safety interface between the specimen and the furnace is provided by Tantalum anti-welding rings. Gatan's Hexring® specimen clamping system is used to securely and precisely hold the specimen and put in the furnace to ensure good thermal contact between the specimen and the furnace. Furnace for low specimen mass ensures a rapid response to changes in the heater current.

Figure 2.9: Heating holder for in situ experiments [10].

Two main parts; namely water recirculator and smart set hot stage heater controller as shown in **Fig. 2.10** (a) and (b), are connected with the TEM heating holder. The specimen temperature rate of increase can be controlled by the smart set hot stage heater controller according to required technique; manually adjusted, or held at any selected temperature for long periods in order to study diffusion processes and precipitation kinetics. It worth to mention that the maximum annealing temperature is 900^{o}C. In addition, water recirculator is needed in order to maintain the temperature at specimen holder close to the specimen stage temperature.

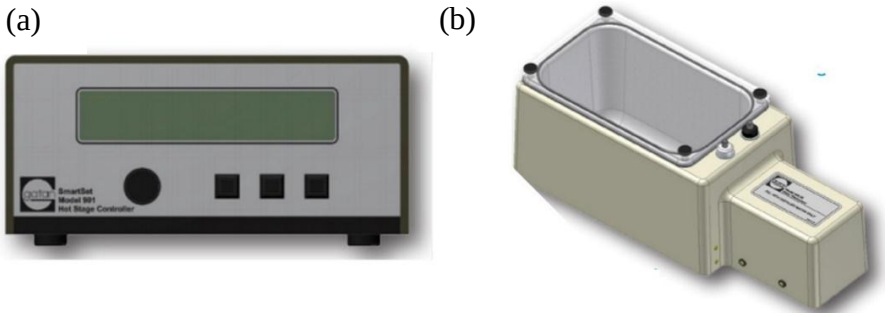

Figure 2.10: The images of (a) smart set hot stage heater controller and (b) water recirculator [10].

2.2.3. Raman spectroscopy

Raman spectroscopy has historically been used to probe structural and electronic characteristics of graphite materials, notably to determine the number of graphene layers by probing the phonon spectrum of graphene [11, 12]. Raman spectroscopy is a relatively easy, non-destructive, no contacting, and quick measurement method to probe the inelastic scattering of light from a sample surface at room temperature at ambient pressure. The wavelength of the bands is affected by the energy of the laser, and the following wavelengths are given for a laser excitation energy of 532.08 nm, in which a NRS-3300 laser Raman spectrometer was used to take the Raman spectra. Three important bands are observed in graphitic materials [13–15].

The graphitic peak around 1582 cm^{-1}, called the G band, is caused by in-plane vibration of sp2 carbon atoms (E2g phonon); the presence of a G band in the Raman spectra indicates that the sample contains sp^2 carbon networks. The signal strength of the D band, located around 1350 cm^{-1} and due to first-order zone boundary phonons, depends strongly on the amount of disorder in the graphitic material [16]; the D band is activated in case of a defect in the network [17, 18]. The third band around 2690 cm^{-1}, called the 2D band as an overtone of the D band, is caused by second-order zone boundary phonons which exhibits a strong frequency dependence on the excitation laser energy and is associated with stacking orders. This 2D band has been used to determine the number of graphene layers [18, 19]. The Full Width at Half-Maximum (FWHM) of 2D bands can be used to determine the number of layers of the considered graphene samples. Monolayer graphene shows a very sharp, symmetric and Lorentzian 2D band. With the increase of a number of layers, the 2D band becomes broader, less symmetric and decreases in intensity: the FWHM increases. The FWHM of the 2D band for a monolayer, bilayer and multilayer graphene could typically be 30 cm^{-1}, 50 cm^{-1}, and 80 cm^{-1}, respectively. The intensity ratio I_{2D}/I_G of the 2D and G bands, respectively, is widely used to characterize the number of layers in the synthesized graphene film. A high ratio indicates monolayer graphene and the lower the ratio, the more layers, with 1 being bilayer graphene and below 1 for multilayer graphene.

2.3. References

[1] M. Tanemura, T. Okita, H. Yamauchi, S. Tanemura, and R. Morishima, Appl. Phys.Lett. **84,** 3831, 2004.

[2] M. Tanemura, T. Okita, H. Yamauchi, S. Tanemura and R. Morishima, Appl. Phys. Lett. **84**, 19, 3831, 2004.

[3] M. Tanemura, H. Hatano, M. Kitazawa, J. Tanaka, T. Okita, S. P. Lau, H. Y. Yang, S. F. Yu, L. Huang, L. Miao, and S. Tanemura, Surface Science. **600**, 3663, 2006.

[4] M. Tanemura, T. Okita, J. Tanaka, M. Kitazawa, K. Itoh, L. Miao, S. Tanemura, S. P. Lau, H. Yang, and L. Huang, IEEE Transactions on Nanotechnology **5**, 587, 2006.

[5] M. Tanemura and S. P. Lau: "Flexible Field Emitters: Carbon Nanofibers (Chapter 15.)" in "Carbon Nanotube and Related Field Emitters: Fundamentals and Applications" Edited by Y. Saitoh, Wiley-VCH Verlag GmbH & Co. KGaA (Weinheim) 2010.

[6] P. E. J. Flewitt, R. K. Wild, Physical Methods for Materials Characterization, IOP Publishing, Bristol, 515, 1994.

[7] B. J. Inkson, Scanning electron microscopy (SEM) and transmission electron microscopy (TEM) for materials characterization, Pages 17-43, 2016.

[8] D. B. Williams and C. B Carter, Transmission Electron Microscopy, Part I: Basics, Springer Science, Second Edition, 3-22, 2009.

[9] M. S. Rosmi, Engineering of Transition Metal-Assisted Graphene and Carbon Nanotubes Formation in Transmission Electron Microscopy (Doctoral dissertation), 2017.

[10] http://mtrmika. Technion .ac. il/ wp-content/uploads/2014/02/652_Double_Tilt_Heat_ Holder_Dsheet_FL5.pdf.

[11] M. A. Pimenta, G. Dresselhaus, M. S. Dresselhaus, L. G. Cançado, A. Jorio, R. Saito, Physical Chemistry Chemical Physics **9**, 1276, 2007.

[12] P. Klar, E. Lidorikis, A. Eckmann, I. A. Verzhbitskiy, A. C. Ferrari, C. Casiraghi, Physical Review B, **87,** 205435, 2013.

[13] Ni Z. Wang, T. Yu, Z. Shen, H. Wang, Y. Wu, W. Chen, A. T. S. W. Wee, The Journal of Physical Chemistry C, **112**, 10637, 2008.

[14] D. Graf, F. Molitor, K. Ensslin, C. Stampfer, A. Jungen, C. Hierold, L. Wirtz, Nano Letters, **7**, 238, 2007.

[15] A. C. Ferrari, J. C. Meyer, V. Scardaci, C. Casiraghi, M. Lazzeri, F. Mauri, S. Piscanec, D. Jiang, K. S. Novoselov, S.Roth, A. K. Geim, Physical Review Letters **97**, 187401, 2006.

[16] A. Eckmann, A. Felten, A. Mishchenko, L. Britnell, R. Krupke, K. S. Novoselov, Nano Letters, **12**, 3925, 2012.

[17] F. Tuinstra, J. L. Koenig, The Journal of Chemical Physics **53**, 1126, 1970.

[18] Y. Zhu, S. Murali, W. Cai, X. Li, J. W. Suk, J. R. Potts, R. S. Ruoff, Advanced Materials **22**, 3906, 2010.

[19] Y. Hao, Y. Wang, L. Wang, Z. Ni, Z. Wang, R. Wang, C. K. Koo, Z. Shen, J. T. L. T. Thong, Small **6**, 195, 2010.

Chapter 3. Graphene Formation Induced by Ar^+ Ion Beam Irradiation: Towards the graphene formation at 150ºC

3.1. Introduction

In this chapter, the first strategy was attempted, namely, validity of another low melting point metal in the low-temperature growth of graphene was verified. For this purpose, indium (In), whose melting point, 156.6ºC, is much lower than Sn, was employed here. As was described in the previous chapters, ion-induced CNFs are amorphous in nature. However, if ion-induced graphene is controllably fabricated, it will be quite fascinating. Up to now, all the reported metal-CNF combinations and metal-covered CNF cases, such as Cu, Fe, Ag, Au, and Pt included CNFs and Cu covered CNFs, showed no graphitized layers in the as-fabricated CNFs [1-4]. They were featured by metal nanoparticles dispersed in amorphous CNF matrix and transferred into graphene and CNT only after the electron current flow (resistive Joule heating) or heating in vacuum [2, 5, 6]. If the In is used as the catalyst, does the graphitized CNFs form without any post heat treatment? This is also the very interesting subject.

3.2. Experimental Section

Indium incorporated carbon nanofibers (In-CNFs) were grown at an edge of graphite foil with a dimension of 25 x 5 x 0.1 mm. **Fig. 3.1** shows a geometrical configuration of graphite foil and In plate, which were mounted on a water-cooled sample holder, for the growth of In-CNFs. The graphite foil edge and the In plate were co-irradiated with Ar^+ ions at 1 keV and 600 eV

for 60 minutes at room temperature, similar to the previous Sn case under the same conditions described in chapter 2.2. After the ion irradiation, the samples were analyzed by SEM and TEM in detail.

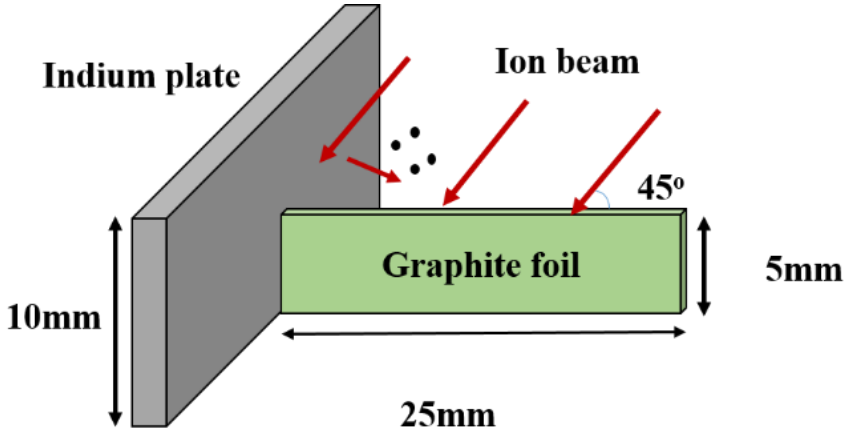

Figure 3.1: Schematic illustration of the experimental setup for the fabrication of In-CNFs**.**

3.3. Results and discussion

After Ar^+ irradiation, the graphite foil at the position of 1.5 cm away from In plate was observed by SEM and TEM. **Fig. 3.2** shows typical SEM images of the graphite foil surfaces after Ar^+ ion irradiation at 600 eV and 1 keV. Both surfaces were covered with CNFs-tipped cones, similar to the previous cases of simultaneous supply of various metals [1-3, 7]. The CNFs were similar in length, 1.5-2.5 μm, for both surfaces, whereas the numerical density was much higher for the surface irradiated at 1 keV (~ 6.8×10^3 /mm^2) compared with that irradiated at 600 eV (~ 3.3×10^3 /mm^2).

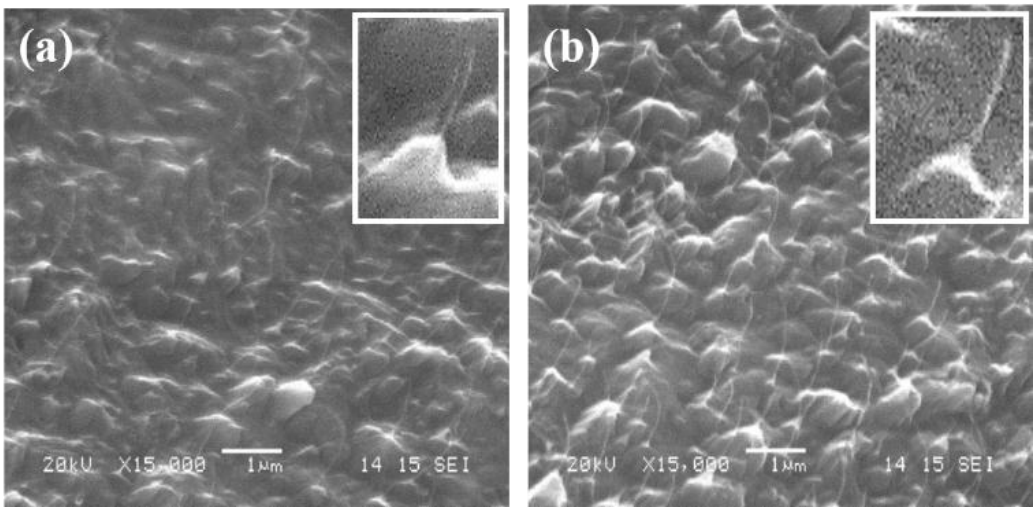

Figure 3.2: SEM images of the surfaces irradiated with Ar^+ ions at (a) 600 eV and (b) 1 keV. Insets: Enlarged SEM images of typical CNF-tipped cones.

TEM images of a typical In-CNF tipped cone fabricated at 600 eV are shown in **Figs. 3.3(a-c)**. **Fig. 3.3(a)** clearly shows that a fibrous structure grew on the tip of a cone base. High-resolution TEM images of squares A (CNF bottom-stem part) and B (cone tip part) in **Fig. 3.3(a)** are shown in **Fig. 3.3(b)** and **3.3(c)**, respectively, disclosing that nanoparticles (nano-crystallites) of dark contrast were dispersed in amorphous matrix. As shown in **Fig. 3.3(d)**, the selected area electron diffraction (SAED) at around the cone tip part including A and B regions consisted of spotty rings corresponding to In (110), (020), and (112) lattice planes together with a weak broad hallow ring of amorphous C. Thus, it is concluded that the nanofiber tipped cone consists of randomly oriented In nanocrystallites dispersed in amorphous C matrix. The composition of the In-CNF tipped cone was also confirmed by energy dispersive x-ray spectrometry (EDX), disclosing that no impurity was present (**Fig. 3.3(e)**). **Fig. 3.4** shows TEM images of a typical In-CNF tipped cone fabricated at 1 keV. High-magnification TEM images of region A in **Fig. 3.4(a)** is shown in **Fig. 3.4(b)**, also **Fig. 3.4(c)** shows high magnification TEM taken at another fiber. Both Figures reveal the graphitized regions. It should be noted that the graphene region was always accompanied by a hollow region. (Examples of the hollow

regions are indicated by arrows in **Figs. 3.4(a–c)**. The graphene region seen in **Fig. 3.4(b)** is rather prominent and consisted of ~6 straight layers, ~ 30 nm in length with an inter-plane spacing of 0.345 nm corresponding to graphite (002) plane. As seen in **Fig. 3.4(c)**, a tiny In nanoparticle was observed in some cones, and it also located at the vicinity of the hollow region. This point will be discussed later. The graphene and hollow regions were covered with amorphous C layers. It should be mentioned that the most of In- CNF tipped cones fabricated at 1 keV was featured with this type of core-shell (graphitized core - amorphous shell) structures.

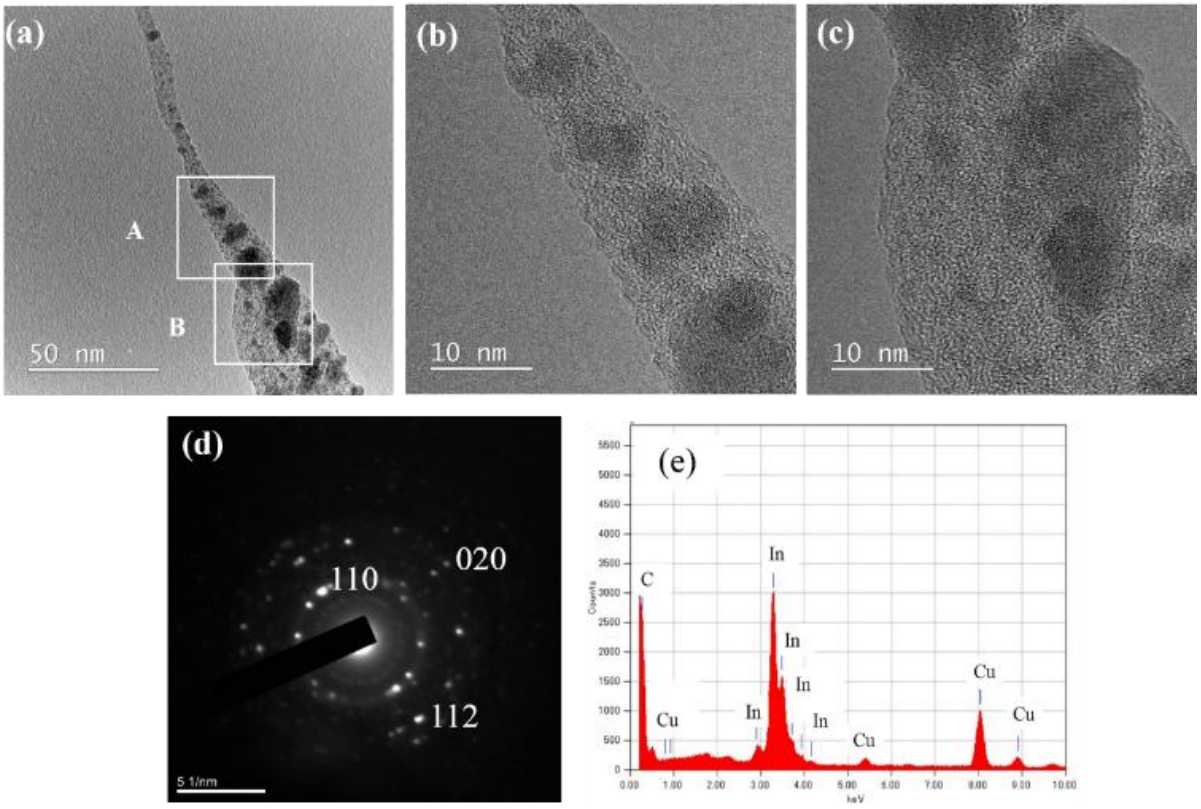

Figure 3.3: (a) Low magnification TEM image of a typical In-CNF tipped cone fabricated at 600 eV, and high-magnification TEM images of (b) region A and (c) region B in (a). (d) SAED pattern at around the cone tip part including A and B regions in (a). (e) EDX spectrum of the In-CNF tipped cone. Detected Cu peak is due to the used Cu TEM mesh.

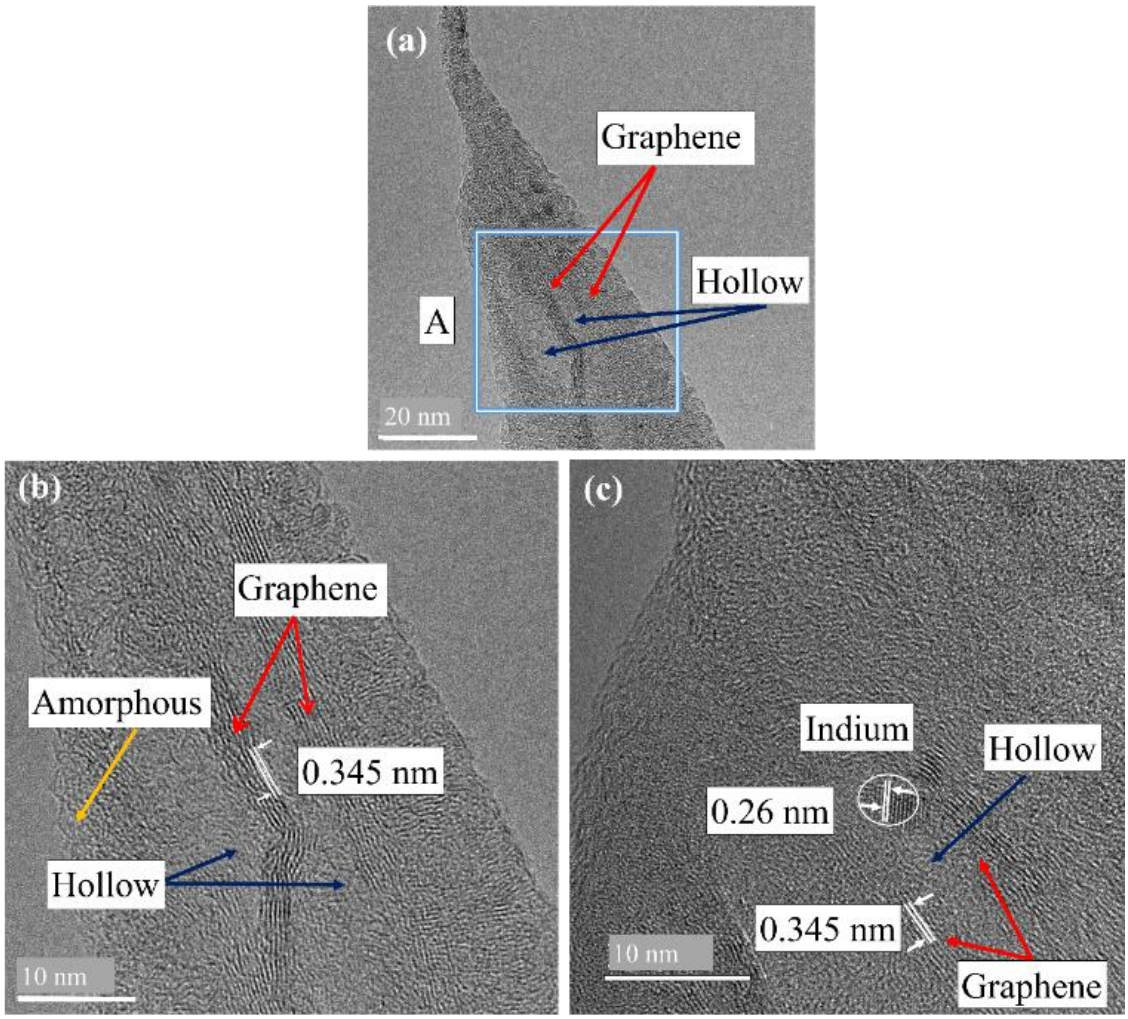

Figure 3.4: TEM images of In-CNF tipped cones fabricated at 1 keV. (b) High magnification TEM image of region A in (a). (c) High magnification TEM image of cone tip part, showing an In nanoparticle (encircled) located at the vicinity of hallow region.

In the previous reports, we have demonstrated that many kind of metals and semiconductors, such as Cu, Fe, Ag, Au, Co, Pt, and Si, can be included into CNFs by simultaneously supplying them during Ar^+ ion irradiation [1-3, 7, 8, 4]. They were always characterized by the CNF-tipped cone in shape and dispersion of metal or semiconductor nanoparticles in the amorphous carbon matrix in crystalline structure, namely no graphene formation, although most of them are well-known as catalysts for CVD graphene and CNT growth. In-CNF tipped cones demonstrated here are the only exception in crystalline nature. The formation of sp^2 bonding is

known to be thermodynamically favorable as compared to other forms of hybridization.[1] This must imply that under a certain circumstance, where carbon atoms move (or displace) readily, sp^2 bonding (namely graphene) tends to form naturally. In fact, it was demonstrated very recently that graphene can form even at the temperature as low as 250°C using Sn, a low melting point (MP) metal catalyst by solid-liquid-solid phase reaction [9]. Carbon atoms in molten metal would meet this condition. MP of bulk In is 156.6°C, and it is also well-known that the smaller the particle size, the lower the MP. It is sometimes dramatic especially for the nanoparticles of less than 10 nm in size [10]. As seen in **Figs. 3.3(b)** and **3.3(c)**, size of In particles included into the amorphous carbon matrix is less than 10 nm in average. Thus, MP of the included In nanoparticles would be much lower than that of the bulk In. So, In nanoparticles would have melted and moved to the base cone part in the case of Ar^+ ion irradiation at 1 keV, whereas the temperature increase during ion irradiation was not so prominent at 600eV.

Thus, in the molten In, graphene would form. And this would be the reason why graphene layers were always accompanied with hollow regions and sometimes residual In nanoparticles located at the vicinity of hollow regions. In the present case, molten In nanoparticles are thought to catalyze the graphitization. In order to confirm this hypothesis and to estimate the necessary temperature for the graphene formation, thin In layer, 100 nm in thickness, and thin amorphous C layer, 50 nm in thickness, was deposited onto SiO_2 covered Si substrates ($In/C/SiO_2/Si$), and the thin film samples thus prepared were simply heated at 150 and 200°C for 60 min under a vacuum condition of 10^{-3} Pa. In order to study the carbon state on the sample surface after heating, Raman analysis was performed.

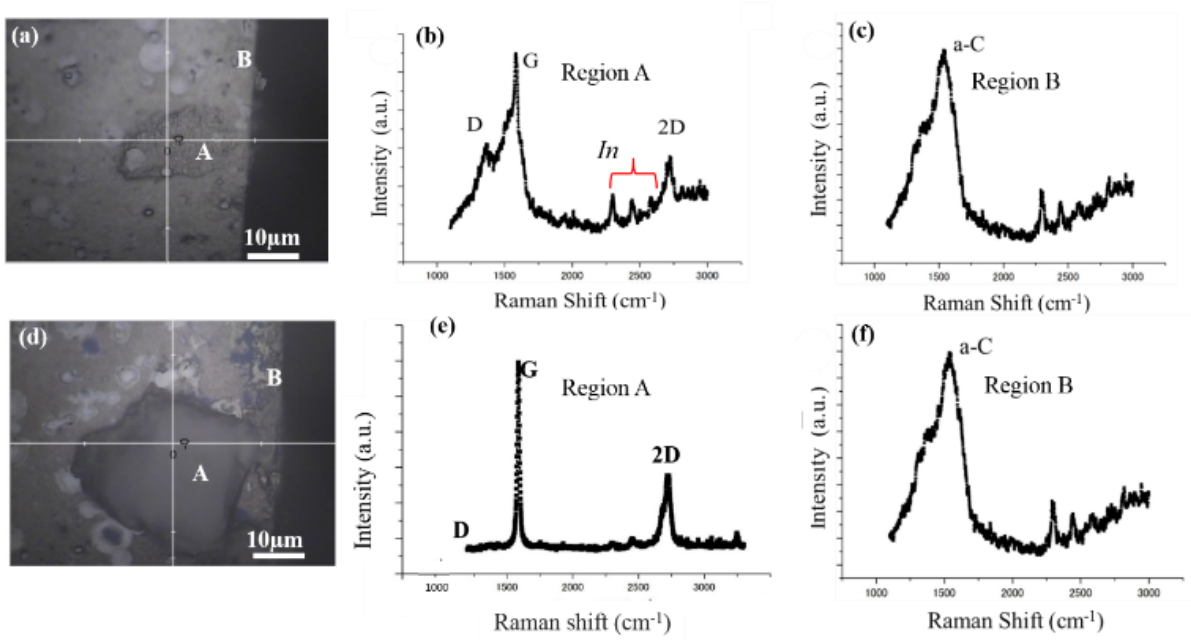

Figure 3.5: (a) Optical microscope image of the thin film sample after heating at 150°C. Raman spectra taken at (b) flake A and (c) surrounding area B in (a). (d) Optical microscope image of the sample after heating at 200°C. Raman spectra taken at (e) flake A and (f) surrounding area B of Fig. (d)**.**

Fig. 3.5(a) presents a typical optical microscope image of the sample surface after heating at 150^{o}C, disclosing that a flake of dark gray contrast (labeled A) is located on the surface. **Fig. 3.5(b)** and **3.5(c)** show Raman spectra attained at the flake (labeled A in **Fig. 3.5(a)** and the surroundings (labeled B in **Fig. 3.5(a)**), respectively. It can be seen that the spectrum of region A consists of intense G and 2D peaks centered at 1583 and 2711 cm^{-1}, respectively, with an intense D peak at 1354 cm^{-1}, revealing the formation of multilayer graphene with defect. The peaks at 2260 and 2725 cm^{-1} are In peaks. Thus, from the Raman spectra, it is concluded that the multilayer graphene formed on the In flake. By contrast, Raman spectrum of region B consisted of a broad peak at about 1550 cm^{-1}, which is a typical amorphous carbon peak, together with In peaks at 2260 and 2725 cm^{-1}, disclosing the amorphous carbon layer on the In film. **Figs. 3.5(d–f)** show a typical optical microscope image and Raman spectra for the thin

film sample heated at 200^{o}C. As seen in **Fig. 3.5(d)**, the surface morphology was similar to that of the 150^{o}C sample, however, a flake (labeled A) formed on the surface was much bigger than that of the 150^{o}C sample. It should be stressed that as seen in **Fig. 3.5(e)**, the sharp and intense G and 2D peaks almost without D peak was detected for region A, clearly indicating the graphene formation of better quality than the 150^{o}C heated sample. Unfortunately, formed graphene did not cover the whole surface, but only on the In flake, as seen in **Fig. 3.5(f)** which discloses the amorphous C and In peaks for surrounding area B, similar to **Fig. 3.5(c)**. Thus, it is concluded that by using In as a catalyst, graphene growth at the temperature as low as 150^{o}C is possible and that higher quality graphene grows at the elevated growth temperature. We are now tackling the optimization of the layer thickness of In and C, and the direct graphene growth onto the flexible polymer substrates. The results will be dealt with the forthcoming papers.

3.4. Conclusions

In summary, it was demonstrated that the graphene formed using Indium as a catalyst for the samples of both room-temperature Ar^{+} irradiated carbon foil and In/carbon stacked films at 150^{o}C in a vacuum. The key of this low-temperature graphene growth was the melting point of the catalyst metal. This finding will open up the synthesis of graphene at further lower temperatures.

3.5. References

[1] M. S. Rosmi, Y. Yaakob, M. Z. Mohd Yusop, S. Sharma, Z. Zulkifli, A. Supee, G. Kalita and M. Tanemura, AIP Adv. **6**, 95109, 2016.

[2] M. Z. M. Yusop, P. Ghosh, Y. Yaakob, G. Kalita, M. Sasase, Y. Hayashi and M. Tanemura, ACS Nano. **6**, 9567, 2012.

[3] Y. Yaakob, M. Z. Yusop, C. Takahashi, G. Kalita, P. Ghosh and M. Tanemura, Jpn. J. Appl. Phys. **52**, 11NL01, 2013.

[4] S. Sharma, M. S. Rosmi, Y. Yaakob, M. Z. M. Yusop, G. Kalita, M. Kitazawa and M. Tanemura, Carbon **132**, 165, 2018.

[5] M. S. Rosmi, M. Z. Yusop, G. Kalita, Y. Yaakob, C. Takahashi and M. Tanemura, Sci. Rep. **4**, 7563, 2014.

[6] M. S. Rosmi, Y. Yaakob, M. Z. Mohd Yusop, S. Sharma, R. Vishwakarma, M. Ibrahim, G. Kalita and M. Tanemura, RSC Adv. **6**, 82459, 2016.

[7] Y. Sugita, M. Kitazawa, M. Zamri M. Yusop, M. Tanemura, Y. Hayashi and R. Ohta, J. Vac. Sci. Technol. B, Microelectron. Nanom. Struct. **27**, 980, 2009.

[8] Y. Yaakob, Y. Kuwataka, M. Z. M. Yusop, S. Tanaka, M. S. Rosmi, G. Kalita and M. Tanemura, Phys. Status Solidi Basic Res. **252**, 1345, 2015.

[9] R. Vishwakarma, M. S. Rosmi, K. Takahashi, Y. Wakamatsu, Y. Yaakob, M. I. Araby, G. Kalita, M. Kitazawa and M. Tanemura, Sci. Rep. **7**, 43756, 2017.

[10] M. Y. Efremov, F. Schiettekatte, M. Zhang, E. A. Olson, A. T. Kwan, R. S. Berry and L. H. Allen, Phys. Rev. Lett. **85**, 3560, 2000.

Chapter 4. Temperature dependence of catalytic activity in graphene synthesis for Sn nanoparticles

4.1. Introduction

In this chapter, a strategy lowering the melting point of the catalyst was attempted by decreasing the catalyst size. Specifically, encouraged by the previous success on the low-temperature growth of graphene using novel Sn catalyst [1], the temperature dependence of the catalytic activity in graphene synthesis for Sn nanoparticles was investigated here based on the detailed observation using TEM. Nevertheless, low-temperature growth should be succeeded for a wider range of applied applications. Therefore, much effort has been devoted to the lower temperature for CVD graphene synthesis. Muñoz et al., for example, have grown monolayer graphene directly on an insulating substrate at 650°C using plasma-assisted CVD. Sulaiman et al. have demonstrated the CVD graphene growth on Cu at 450^{o}C by using chlorobenzene and benzene as a carbon source [2, 3]. Rummeli et al. have achieved the CVD graphene growth at 325°C on insulators using acetylene as a carbon source. Jang et al. reported graphene formation at 100-300 °C using benzene as a carbon source in a CVD process [4, 5]. Very recently, the low-temperature graphene growth using novel catalysts, which have been rarely used for the conventional CVD, were successfully attempted. Fujita et al. and Park et al. employed Ga and Ti, respectively, to achieve the CVD graphene growth at the temperatures lower than 150^{o}C [6, 7]. In our previous papers also, we demonstrated the graphene growth just by the simple vacuum annealing of the stacked C and catalyst films on insulator substrates

at 250 and 150^{o}C for Sn and In catalysts, respectively, both of which are low melting point metals [1, 8]. So, melting point seems to play an important role in the low-temperature graphene growth. In order to understand the graphitization process for those low-melting point metals, detailed observation of the catalyst behavior in (TEM) will be important. In this report, I will deal with the newest findings on this interesting subject, leading to an additional strategy to achieve lower temperature graphene growth.

4.2. Experimental Section

For the TEM observation, sample preparation is quite important. So, samples should be thin enough for the transmission of the incident electrons. To fulfil this prerequisite, we employed the ion-induced CNFs as described in chapter 2. Ion irradiation onto carbon and carbon coated materials is known to induce the formation of CNF tipped cones (conical structures) without any catalyst even at room temperature [9, 10]. Single CNFs grow on respective cone tips, and a variety of the "second" elements can be readily included into CNFs during the CNF growth by a simultaneous supply of metals and semiconductors during the ion irradiation [11-13]. Using this technique, Sn-CNFs were fabricated on an edge of a commercially available graphite substrate (carbon foil) with a thickness of 100 μm at room temperature. **Fig. 4.1(a)** shows a schematic arrangement of a carbon (graphite) foil, 25 x 5 x 0.1 mm^3 in size was mounted on a sample stage, onto which Sn-CNFs grow, and a Sn platelet for the Sn supply source placed perpendicular to the edge of the carbon foil.

Ion irradiations onto Sn substrate and carbon (graphite) foil at 1keV were performed at the room temperature for 60 minutes. The ion irradiation was carried out at an incident angle of 45^{o} with respect to the surface normal to the carbon foil by using Kaufman type ion gun with the ion beam diameter of 6 cm (ION TECH. INC Ltd., model 3-1500-100FC) as described in chapter 2.2.1. The basal and working pressures for the fabrication of the Sn-CNFs were 1.5 x

10^{-5} and 2 x 10^{2} Pa, respectively. After the ion-irradiation, the surface morphology and crystalline structure of the Sn-CNFs were observed by scanning electron microscopy (SEM, JEOL JEM-5600) and TEM at 200 keV (JEM ARM 200F), respectively. Since the respective Sn-CNFs were quite tiny, the characterization of the graphitization was done by TEM, but not by Raman spectroscopy. For the TEM analyses, the Sn-CNF grown carbon foil was cut into three small pieces to anneal them separately at 180, 200 and 250^{o}C in vacuum (ULVAC – Riko MILA – 3000 especially equipped with a turbo-molecular pump) for 1 hr in 4.0~5.6 x 10^{-2} Pa. After cooling down to room temperature from the respective annealing temperatures, the annealed samples were mounted on a TEM sample holder without any post-treatment. Needless to say, in order to determine the temperature dependence of the catalytic activity of Sn, the identical sample should be repeatedly observed after the annealing at various temperatures inside TEM. We tried also this method. However, the element in interest in this study is carbon, so the artifact of carbon contamination should be avoided very carefully. Very unfortunately, carbon contamination induced by TEM electron beam and/or by in-situ TEM heating was not avoidable for the repeated TEM observation of the identical sample position. So, we had to employ the above-described alternative method. Additionally, as synthesized and annealed samples were subjected to X-ray photoelectron spectroscopy (XPS) (PHI 5000 VersaProbe III) and Raman characterizations (NRS 3300 laser Raman spectrometer with laser excitation energy of 532.08 nm).

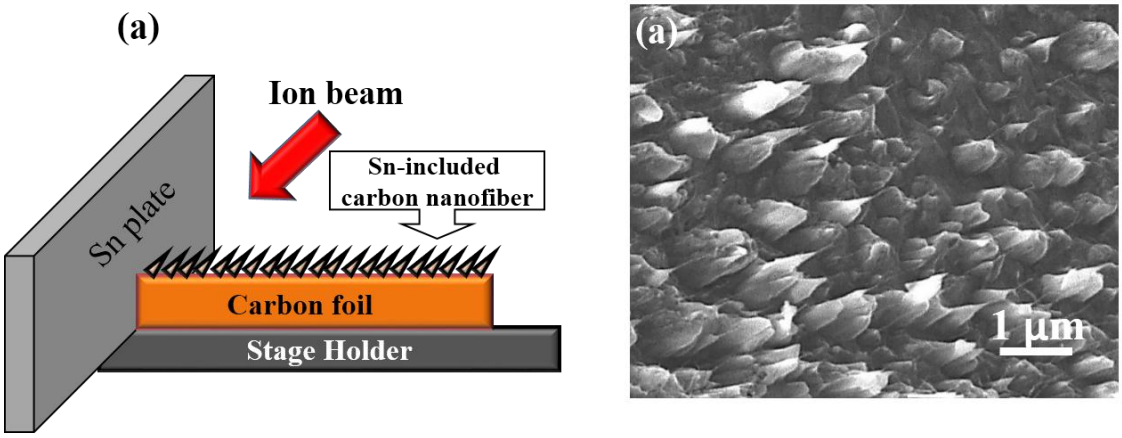

Figure 4.1: a) Schematic diagram of the experimental setup for the fabrication of Sn-CNFs. b) Typical SEM image of Sn-CNF tipped cones fabricated on an edge of a carbon foil.

4.3. Results and discussion

Fig. 4.1(b) shows a typical SEM image of the surface of a carbon foil edge after the ion irradiation. The surface was covered with densely distributed CNF-tipped cones. The cones were about 0.5 and 1 μm in base diameter and length, respectively, and a tiny CNF grew on the respective cone tips. CNFs and cones were pointed in the ion beam direction. The number density of the cones is estimated to be ~ 4.2×10^{3} mm^{-2}.

Fig. 4.2 shows typical TEM images of a tip region of an as-fabricated CNF-tipped cone. As shown in **Fig. 4.2(a)** the fibrous structure grew on a tip of a cone and many darker contrast particles were dispersed in both the nanofiber and the cone tip. High magnification TEM images of squares X (CNF part) and Y (cone tip part) of **Fig. 4.2(a)** are shown in **Fig. 4.2(d)** and **4.2(b)**, respectively. The inset of **Fig. 4.2(b)** shows a metal particle with a lattice spacing of 0.282 nm embedded in amorphous C (referred to a-C) matrix, which corresponds to the spacing of Sn (200) plane [14].

As seen in **Fig. 4.2(d)**, darker contrast Sn nanoparticles of 2-4 nm in size [exemplified by circle A in **Fig. 4.2(d)**] were dispersed in the amorphous carbon matrix. Some of the nanoparticles

agglomerated as indicated by circle B in **Fig. 4.2(d)**. The composition of the Sn-CNF tipped cones was confirmed by energy dispersive X-ray spectrometry (EDS), revealing that no foreign impurity was included as shown in **Fig. 4.2(c)**.

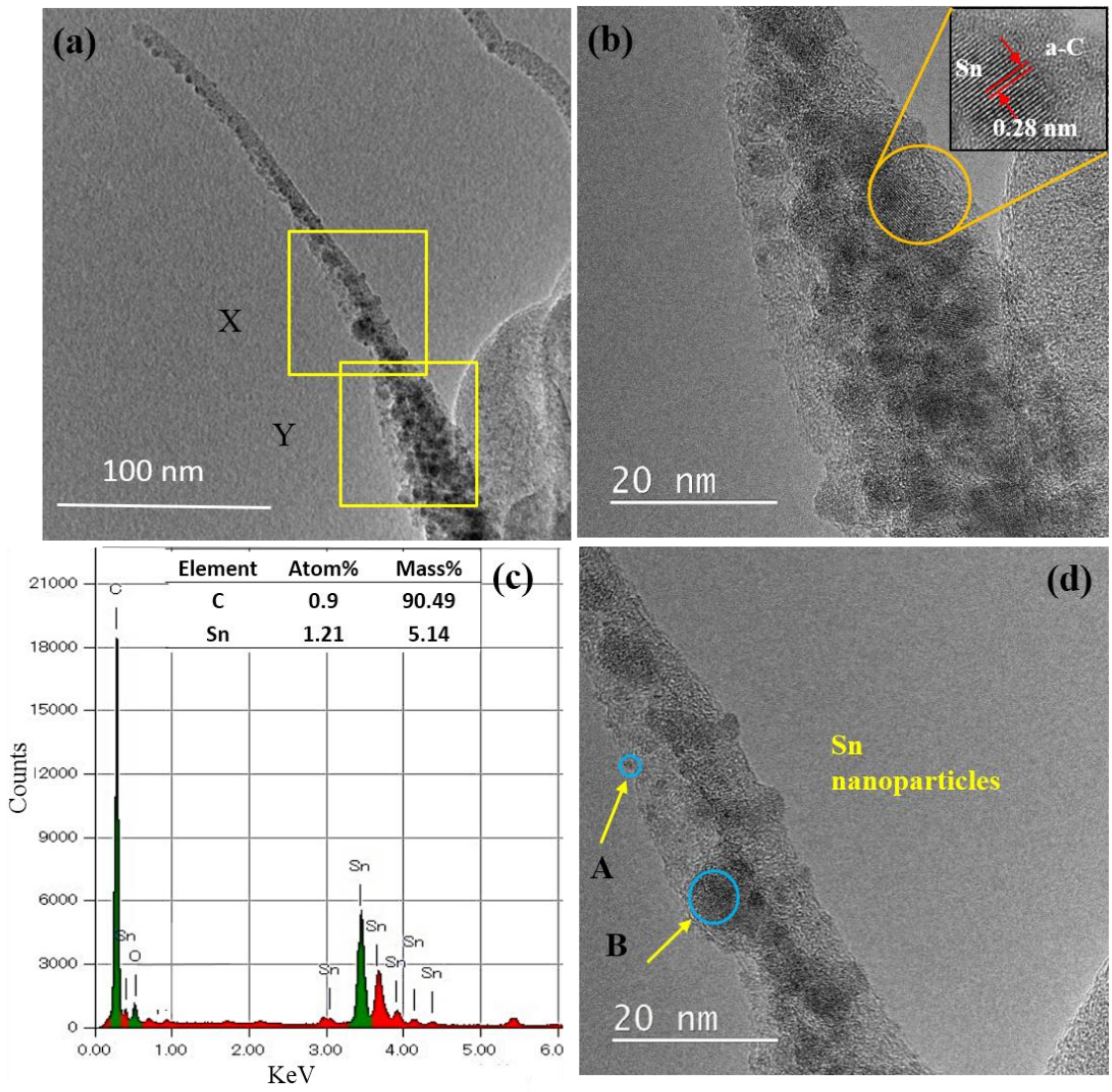

Figure 4.2: (a) Low magnification TEM image of a typical as-fabricated Sn-CNF tipped cone, (b) high magnification TEM image of the region Y in (a), and (c) EDS spectrum of the fiber part of the Sn-CNF, revealing that it was composed of Sn and C. Detected Cu peak is due to a Cu TEM mesh. (d) A high magnification TEM image of the region X in (a), clearly showing the Sn nanoparticles.

Sn-CNF tipped cones were then annealed at various temperatures of 180-250^{o}C for 1 hr in a vacuum. **Fig. 4.3(a)** shows a low magnification TEM image of a typical Sn-CNF tipped cone annealed at 180^{o}C. At a glance, further agglomeration of Sn nanoparticles seemed to occur especially at the inner region of the fiber as indicated by arrows in **Fig. 4.3(a). Fig. 4.3(b)** shows a high magnification image of the rectangular region X in **Fig. 4.3(a)**. Compared with the inner region of the cone, Sn nanoparticles were less prominent at the outer region of the cone as seen in the region X, though the Sn nanoparticles still existed as exemplified by a circle in **Fig. 4.3(b)**. It should be stressed that a careful inspection disclosed the partial graphitization in the region X. The graphitization is much more prominent at the rectangular part Y in **Fig. 4.3(a)** (tip region of the Sn-CNF), as seen in **Fig. 4.3(c).** The lower inset in **Fig. 4.3(c)** shows an intensity line profile of the lattice image, indicating the periodicity of 0.362 nm [see also the upper inset in **Fig. 4.3(c)**]. The lattice spacing is slightly larger than that of the graphene (002) lattice, maybe due to the imperfection of the graphitization. Similar partial graphitization was observed also for the sample annealed at 200^{o}C in a vacuum.

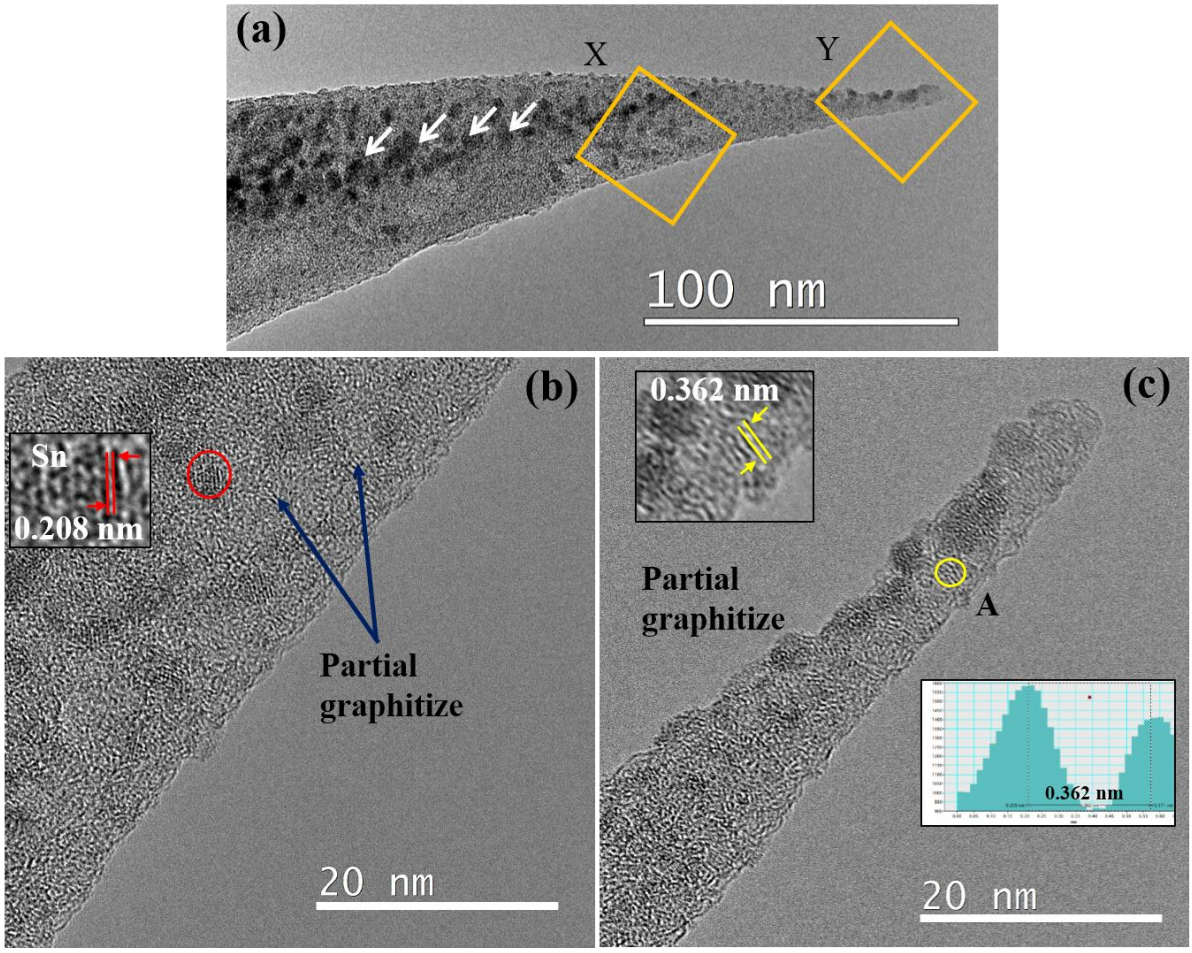

Figure 4.3: (a) Low magnification TEM image of a Sn-CNF tipped cone after annealing at 180^{o}C. (b) A high magnification TEM image of region X in (a), with an inset showing the lattice image of a Sn nanoparticles. (c) A high magnification TEM image of region Y in (a). Upper inset: Enlarged image of circled areas A. Lower inset: intensity line profile of the lattice image of the circle A, indicating the interlayer spacing of 0.362 nm.

Higher temperature is known to facilitate better graphitization by providing enough energy for the structural transformation and mobility of C atoms. As the melting point of bulk, Sn is 231.93°C, heating at 180^{o}C would not be enough to induce the thorough structural change for C-Sn composite. So, investigation of the temperature dependence of the graphitization, namely,

its annealing at a higher temperature will be interesting. **Fig. 4.4** shows the TEM images for a Sn-CNF tipped cone after annealing at 250^{o}C. At a glance, compared with the 180^{o}C annealed sample [**Fig. 4.3(a)**], the number density of black contrast nanoparticles, Sn nanoparticles, decreased. Sn nanoparticles seemed to disappear at near-outer region of the Sn-CNF, whereas at the inner region of the Sn-CNF they still remained, as indicated by arrows and particle agglomeration occurred as indicated by arrow-heads in **Fig. 4.4(a)**. **Fig. 4.4(c)** shows the typical magnified images taken at inner [A and B in **Fig. 4.4(b)**] and near-outer [C and D in **Fig. 4.4(b)**] regions of the Sn-CNF, respectively. In the magnified images, lattice fringes with an interlayer spacing of 0.341nm, corresponding to graphite (002), are observed at both near-outer region and at around nanoparticles in the inner region. It should be noted that the lattice fringes aligned almost in the radial direction of the Sn-CNF except at the Sn nanoparticle as shown in A and B (dark contrast regions) in **Fig. 4.4(c)**.

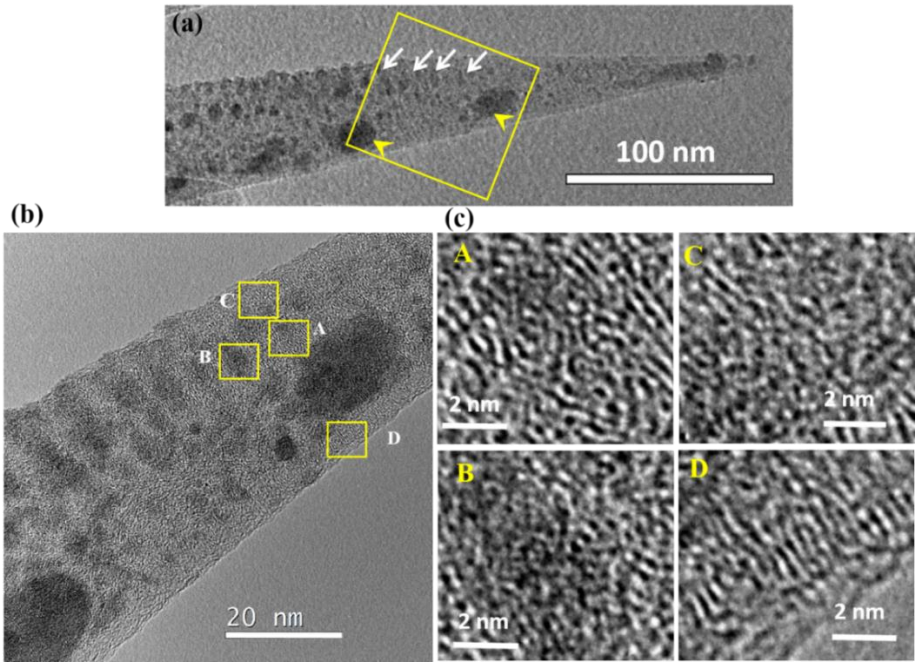

Figure 4.4: (a) Low and (b) medium magnification TEM images of a typical Sn-CNF annealed at 250^{o}C. (c) [A-D in (c)] high magnification TEM images of respective regions A-D in (b).

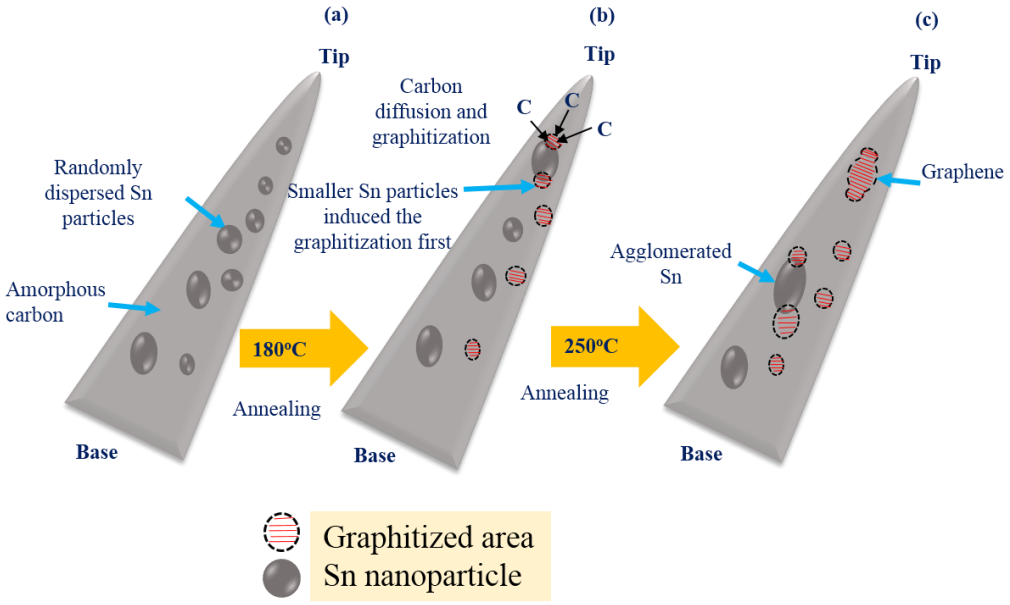

Figure 4.5: Schematic representation of the graphene formation during heating in vacuum. (a) Initial structure of Sn-CNF before heating, (b) annealing at 180°C and (c) annealing at 250°C.

Based on the above described TEM observations, the transformation mechanism of amorphous carbon to the graphitic structure under heat treatment would be explained schematically as shown in **Fig. 4.5**. For the as-grown Sn-CNFs, Sn nanoparticles of about 2-4 nm in diameter are distributed both at near-outer and inner regions of the amorphous fibers and some of the nanoparticles are already agglomerated. During the heating at 180°C, the gradual agglomeration occurred especially for the smaller particles due to the partial melting of Sn nanoparticles. Simultaneously, carbon atoms diffuse into Sn nanoparticles. In the molten stated of the matrix (Sn), carbon atoms would rearrange into graphitized structure easily to form the partial graphitization as shown in **Fig. 4.5(b)** and **(c)**. At higher temperatures, evaporation also would occur as well as melting and the agglomeration that would accelerate the graphitization. As was mentioned above, the lattice fringes aligned almost in the radial direction of the Sn-CNF. This is totally different from other catalyst cases, such as Cu, Fe and Pt commonly used in CVD for the graphene and CNT growth [11, 12,16]. For the CNFs including Fe and Pt

nanoparticles, graphitization occurred like an outer-peel formation of the CNF, namely, transformation from CNF to multilayer CNTs occurred [15, 17], whereas, for Cu-included and Cu-coated CNFs, graphene flakes formed [11,15], after their resistive Joule heating. In those cases, graphite lattice fringes aligned along the stem direction of the CNFs. For the CNFs including Ag and Au nanoparticles, metal-core and graphitic-shell structure formed in the CNFs after their resistive Joule heating [13]. For Sn case presented here, movement of Sn nanoparticles in the radial direction would be responsible for the graphitization direction.

To study the effect of temperature on graphitization process, X-ray photoelectron spectroscopy (XPS) measurement was carried out for the annealed samples. **Fig. 4.6 (a)** and **(b)** shows the XPS spectra of the samples heated at 180^{o}C and 250^{o}C respectively. It is clearly observed that sample annealed at 250^{o}C show sharp C peak with a value of 284.4 eV corresponding to SP^2 carbon as reported in other work [18]. Whereas the sample annealed at 180^{o}C show broader C peak with presence of an extra peak at 288 eV. Presence of broad C peak indicates the presence of other C-O and C=O radicals in the sample. XPS data concludes, significantly the better graphitization of the sample annealed at 250^{o}C compared to that of 180^{o}C. Further, annealed samples along with as-synthesized samples (un-annealed samples) are also characterized using Raman spectroscopy, which has become a standard measurement technique for studying the quality of graphene in recent years. **Fig. 4.6 (c)** presents the corresponding Raman spectra of the samples before and after annealing at 180 & 250^{o}C. Typical Raman modes of the D, G, and 2D bands are studied to confirm the quality of the graphene. It is observed that un-annealed samples show no distinguishable G peak with no presence of 2D peak, indicating the presence of amorphous C. Whereas the sample annealed at 180^{o}C shows the clear G peak along with distinguishable D and 2D peak. Presence of 2D peak indicates presence of graphitized C in the sample. Sample annealed at 250^{o}C show clear presence of D, G, and 2D peak. Presence of

intense 2D peak indicates the presence of highly graphitized C. This result is in close agreement with the results obtained from the TEM observation.

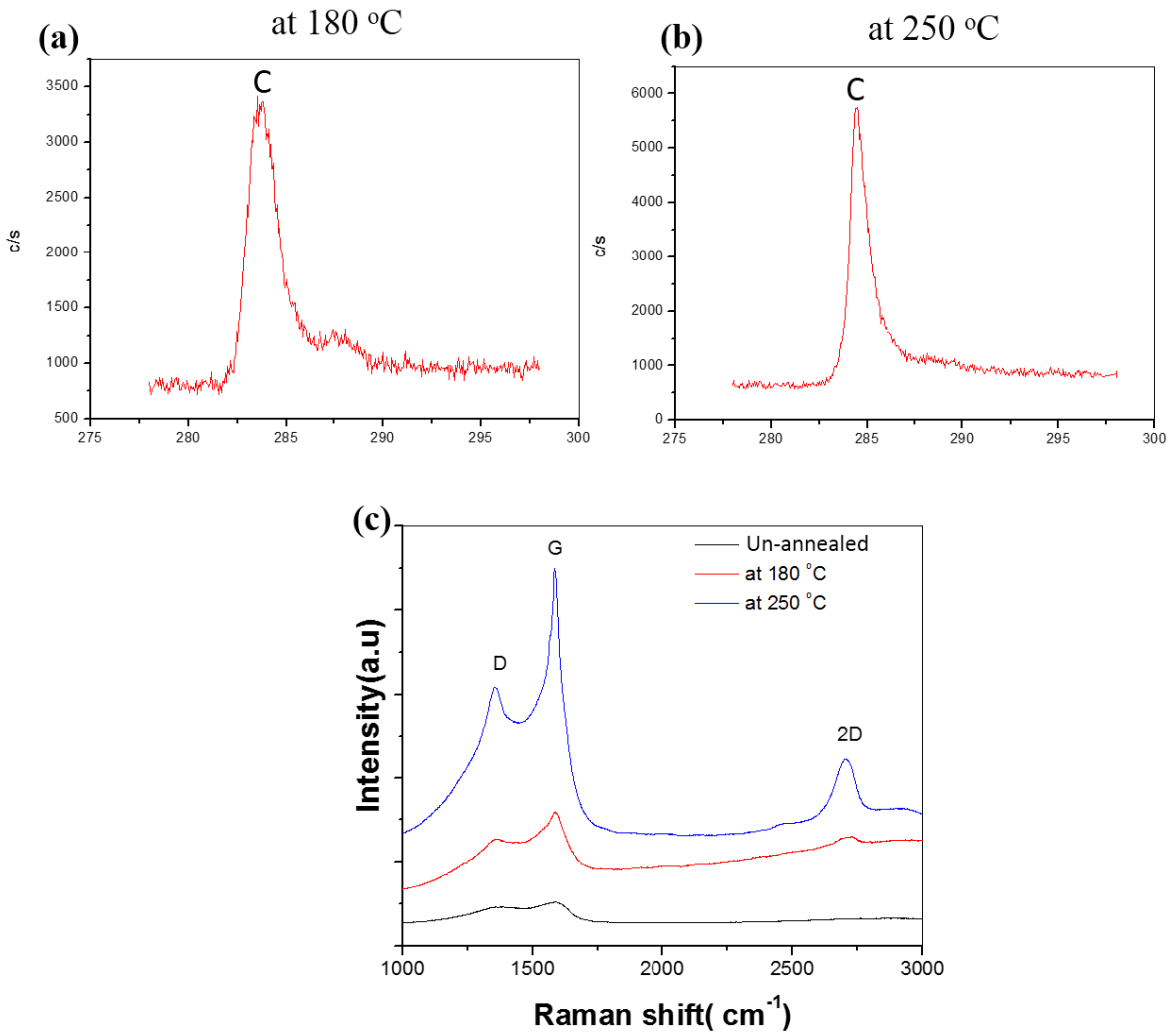

Figure 4.6: (a) XPS spectra of Sn-CNF annealed at 180°C and (b) 250°C (c) Raman spectra of the un-annealed and the annealed samples 180°C and 250°C.

Another important aspect beside the graphitization temperature is the electrical property of the synthesized graphitized samples. Sn-CNF as-fabricated was subjected to the current-voltage (I-V) measurement inside TEM. **Fig. 4.7 (a)** shows a typical I-V characteristic of the sample

measured by using a W probe in two-probe method, revealing the Ohmic (metallic) property of the sample. **Fig. 4.7 (b)** shows a magnified TEM image of the sample after the I-V measurement, disclosing the clear graphitization without any residual Sn nanoparticles. Assuming the cross-section area of the CNF is circular, the current density at the thinnest part reached ~7.1 x 10^7 A/cm^2, which is almost comparable with that of graphene nanowire consisting of the agglomerated graphene flakes, [11] and will be enough for the interconnection applications.

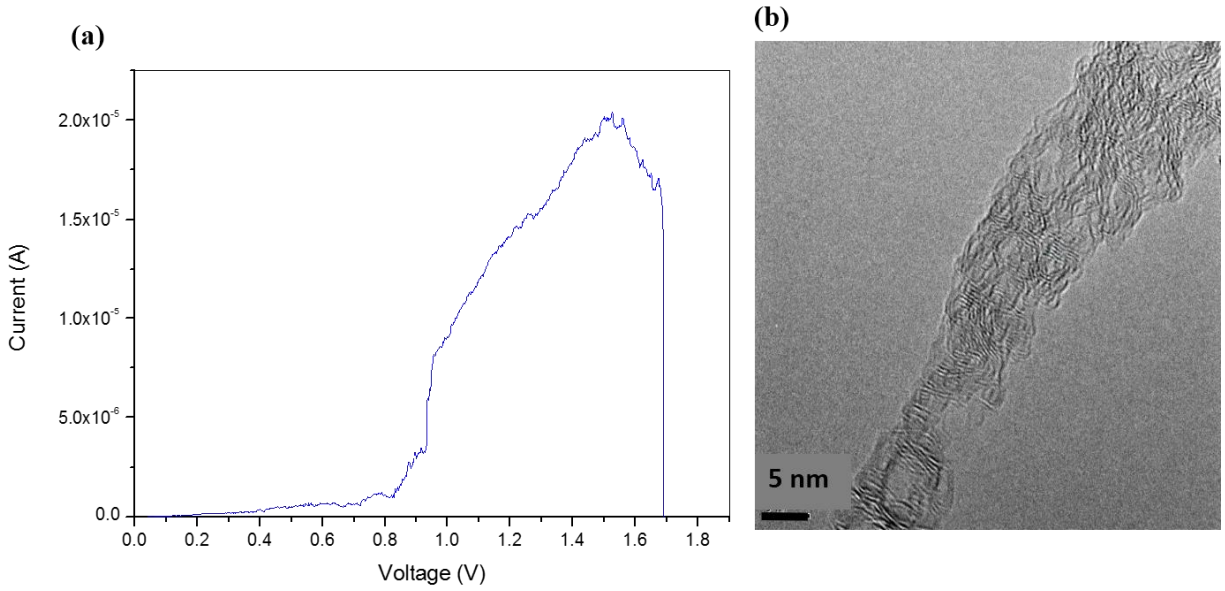

Figure 4.7: (a) I-V characteristic of a Sn-CNF measured in TEM. (b) High-magnification TEM image showing the formation of graphitic layers.

4.4. Conclusions

In conclusion, TEM and Raman spectra observation clearly demonstrated that the graphitization started to occur at the temperature as low as 180^{o}C for Sn nanoparticles due to the decrease in the melting point for nanoparticles. The combination of low melting point metal and its nanoparticle form would be the new strategy for the lower temperature graphene growth.

4.5 References

[1] R. Vishwakarma, M. S. Rosmi, K. Takahashi, Y. Wakamatsu, Y. Yaakob, M. I. Araby, G. Kalita, M. Kitazawa and M. Tanemura, Sci. Rep. **7**, 43756, 2017.

[2] K. Sulaiman, A. Y. Ali, D. Elkington, K. Feron, K. F. Anderson, W. Belcher, P. Dastoor and X. Zhou, Carbon **107**, 325, 2016.

[3] R. Muñoz, C. Munuera, J. I. Martínez, J. Azpeitia, C. Gómez-Aleixandre, and M. García-Hernández, 2D Mater **4**, 15009, 2017.

[4] M. H. Rümmeli, A. Bachmatiuk, A. Scott, F. Börrnert, J. H. Warner, V. Hoffmann, J.-H. Lin, G. Cuniberti and B. Büchner, ACS Nano **4**, 4206, 2011.

[5] J. Jang, M. Son, S. Chung, K. Kim, C. Cho, B. H. Lee, and M. Ham, Sci. Rep. **5**, 17955, 2015.

[6] J. I. Fujita, T. Hiyama, A. Hirukawa, T. Kondo, J. Nakamura, S. I. Ito, R. Araki, Y. Ito, M. Takeguchi and W. W. Pai, Sci. Rep.**7**, 12371, 2017.

[7] B.-J. Park, J.-S. Choi, J.-H. Eom, H. Ha, H. Y. Kim, S. Lee, H. Shin, and S.-G. Yoon, ACS Nano **12**, 2008, 2018.

[8] M. I. Araby, M. S. Rosmi, R. Vishwakarma, S. Sharma, Y. Wakamatsu, K. Takahashi, G. Kalita, M. Kitazawa and M. Tanemura, RSC Adv. **7**, 47353, 2017.

[9] M. Tanemura, M. Kitazawa, J. Tanaka, T. Okita, R. Ohta, L. Miao, and S. Tanemura, Jpn. J. Appl. Phys., 2006, **45**, 2004, 2006.

[10] M. Tanemura, J. Tanaka, K. Itoh, Y. Fujimoto, Y. Agawa, L. Miao and S. Tanemura, Appl. Phys. Lett., **86**, 113107, 2005.

[11] M. S. Rosmi, Y. Yaakob, M. Z. Mohd Yusop, S. Sharma, R. Vishwakarma, M. I. Araby,

G. Kalita, and M. Tanemura, RSC Adv. **6**, 82459, 2016.

[12] M. Z. M. Yusop, P. Ghosh, Y. Yaakob, G. Kalita, M. Sasase, Y. Hayashi and M. Tanemura, ACS Nano **6**, 9567, 2012.

[13] Y. Yaakob, M. Z. Mohd Yusop, C. Takahashi, M. S. Rosmi, G. Kalita and M. Tanemura, RSC Adv. **5**, 5647, 2015.

[14] S. Li, X. Zhong, Y. Song, X. Shen, J. Sun, Y. Song, R. Wang, M. Zhu, H. Zhong, and A. Zheng, J. Mater. Chem. C **2**, 7687, 2014.

[15] M. S. Rosmi, M. Z. Yusop, G. Kalita, Y. Yaakob, C. Takahashi and M. Tanemura, Sci. Rep. **4**, 7563, 2014.

[16] S. Sharma, M. S. Rosmi, Y. Yaakob, M. Z. M. Yusop, G. Kalita, M. Kitazawa and M. Tanemura, Carbon **132**, 165, 2018.

[17] C. Takahashi, Y. Yaakob, M. Z. Mohd Yusop, G. Kalita and M. Tanemura, Carbon **75**, 277, 2014.

[18] F.T. Johra, J.W. Lee, W.G. Jung, Facile and safe graphene preparation on solution based platform, J. Ind. Eng. Chem. **20**, 2887, 2014.

Chapter 5. Development of oxide nanofiber tipped cantilever as a substrate for cross sectional transmission electron microscopy analysis

5.1. Introduction

As shown in the previous chapters, TEM is a powerful tool for the material analysis in atomic scale. The next step in my research will be the dynamic observation of the catalytic behavior on the substrate, namely, the in-situ observation of the graphene formation at the interface between catalysts and an insulator substrate by TEM, especially by cross sectional TEM (X-TEM). For TEM analyses, samples should be thin enough for the transmission of the incidence electrons. This requirement makes the sample preparation time-consuming and complicated in general. For X-TEM observations, samples are generally prepared by ion milling of the mechanically pre-thinned materials in question, such as multilayered thin films, or by thinning the desired region of the materials in question using a focused ion beam [1-3]. In both methods, thinning process using ion beam is employed after the synthesis of the materials, and hence a care to the ion-induced damage to the specimen should be paid. For the dynamic observation of the graphene formation process at the interface, such a post thinning process is not applicable. Thus, the development of simple and damage free sample preparation technique for X-TEM is indispensable.

As described in the previous chapters, ion-induced CNF-tipped cones are readily formed on a

foil edge [4-7] and they are ready for the TEM analyses without any post-treatment [8-12]. This implies that nano-fibrous samples are quite suitable for TEM analyses. If oxide nano-fibrous samples are fabricatable, it will be fascinating as substrates for X-TEM analyses, because oxide, such as SiO_2, is a well-known substrate for the thin film deposition and is tolerant against the post-treatment process under various environments, such as post-annealing for diffusion and diffusion barrier experiments. In the ion-induced CNF growth, a variety of elements, such as Fe, Au, Ag, Cu, Pt, and Si, can be included into CNFs during the CNF growth by a simultaneous supply of metals and semiconductors during the ion irradiation [9-17]. Based on this technique, in this chapter, the fabrication of Si oxide nanofibers (SONs) as substrates for X-TEM analyses was challenged for the future X-TEM analyses of the low-temperature graphene formation at the interface between the catalyst and the SiO_2 substrate.

5.2. Fabrication of Si Oxide Nanofibers (SONs) and thin film

5.2.1. Deposition thereon

Fig. 5.1 shows a schematic representation of the ion-induced CNF growth on a tip of a conical protrusion. A detailed mechanism of the ion-induced CNF growth is described in chapter 2 [4-7]. In brief, (i) re-deposition of carbon atoms sputter-ejected from the surface onto the sidewall of the conical protrusions, (ii) the surface diffusion of the re-deposited carbon atoms towards the tip of the respective cones during ion irradiation, and hence (iii) forming a CNF. As described above, in this CNF growth, various kinds of metals and semiconductors can be supplied to fabricate composite CNFs. In the present work, Si was supplied during the CNF growth to fabricate Si-included CNFs (Si-CNFs) as the first step to SONs. SON itself (10-100 nm in diameter and less than 1 μm in length) is quite difficult to handle. So, a proper substrate onto which the SON grows is indispensable for the following thin film deposition and the transfer to TEM. For this purpose, we conveniently employed commercially available Si

cantilevers (OMCL-AC160TS; Olympus) for atomic force microscope (AFM) as the substrate here, because pristine CNFs (without any metal or semiconductor inclusion) are known to grow onto such Si and Si-based cantilevers simply by the Ar^+ ion irradiation onto carbon pre-coated cantilevers [17-21].

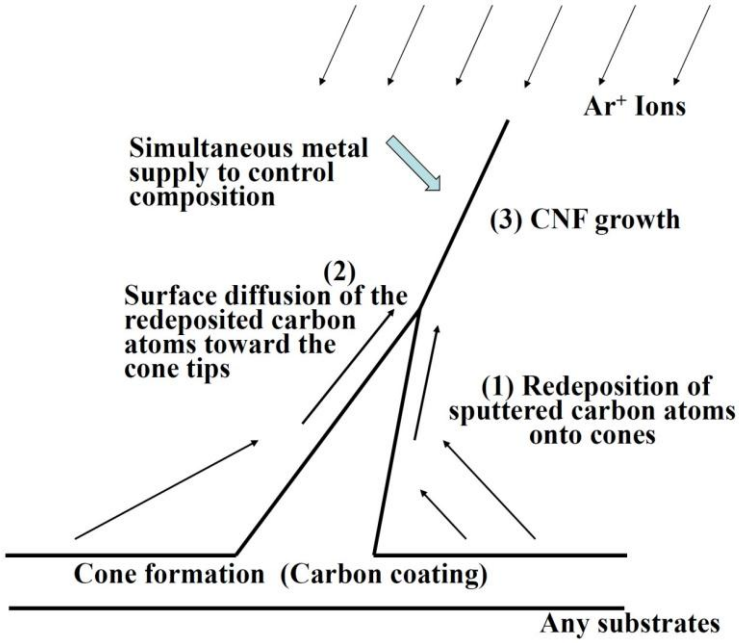

Figure 5.1: Schematic representation of the growth mechanism of ion-induced CNF [7]

Si supply to fabricate Si-CNFs was done by the 600 eV Ar^+ ion irradiation onto both the cantilevers and a Si plate located near the cantilevers using a Kaufman-type ion source (Ion Tech, 3-1500-100FC), 3 cm in ion-source diameter. The basal and working pressures were less than $5x10^{-4}$ and $5x10^{-2}$ Pa, respectively. 3-5 chips of cantilevers were processed in one batch. The cantilever was then annealed ex-situ at 1000^{o}C in an atmospheric ambient for 1 hour to form a Si-oxide nanofiber (SON) on the tip of the cantilever [see **Fig. 5.2(a)**]. For the structural and morphological characterization of the SON tipped cantilevers, TEM [JEM-ARM200F (JEOL)] and SEM [JSM-5600 (JEOL)] were used, respectively.

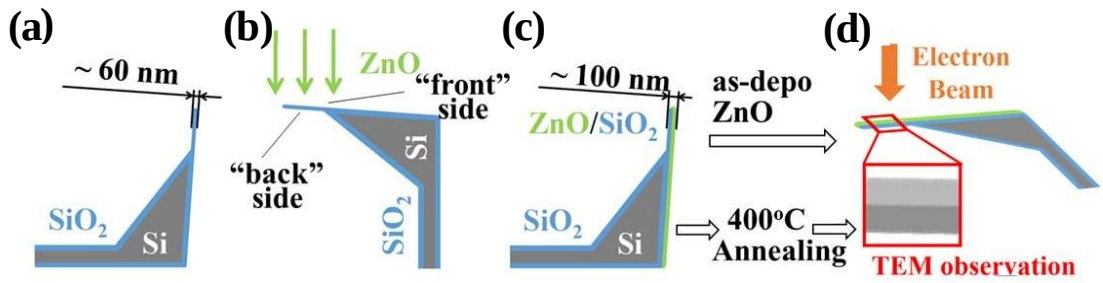

Figure 5.2: Schematic representation of (a) SON fabrication, (b) ZnO film deposition onto the SON, (c) ZnO/SON sample for X-TEM, and (d) X-TEM observation.

By using the SON tipped cantilevers, ZnO films, ~22 nm thick, deposited by an arc plasma deposition (APD) method were analyzed by TEM (X-TEM analyses). APD method is sometimes successfully used for the deposition of novel metal nanoparticles and thin films [22-24], and ZnO powders synthesized using arc discharge sometimes show the p-type property [25]. So the APD deposited ZnO will be fascinating depending on the application. In the present work, the ZnO deposition using a metal Zn target was carried out at room temperature [see **Fig. 5.2(b)** and **2(c)**] using an APD source [ARL-300 (ULVAC-RIKO)] under working pressure of 10 Pa. A Zn target employed was the commercially available polycrystalline metal Zn rod (ZN-482652, The Nilaco Corporation, purity > 99.99%). The applied voltage for APD was fixed to 80 V. Some of the samples were further post-annealed at 400^{o}C for 3.5 hours in atmospheric ambient for the grain growth of the ZnO. The prepared ZnO film samples were mounted onto a TEM sample holder without any post-treatment and then were observed in the cross-sectional direction to obtain X-TEM images [**Fig. 5.2(d)**] using JEM-ARM200F (JEOL).

5.3. Results and discussion

5.3.1. Characterization of SON tipped cantilevers

Prior to the X-TEM observation of ZnO films, SON tipped cantilevers prepared by annealing

of Si-CNF tipped cantilevers were characterized by TEM. **Fig. 3(a)** shows a SEM image of a typical SON tipped cantilever thus prepared. The formed SON was linear in shape with ~90 and ~500 nm in diameter and length, respectively.

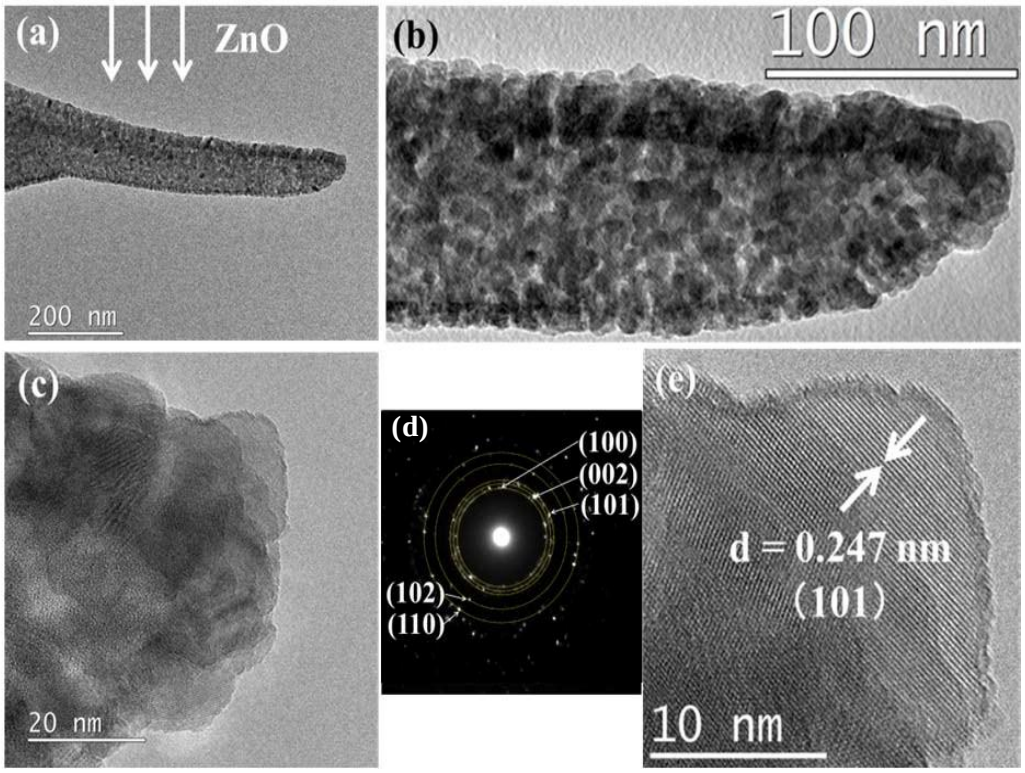

Figure 5.3: Characterization of a SON tipped cantilever. (a) SEM image, (b) low and (c) high magnification X-TEM images of a tip region of the SON. (d) EDP of the SON. (e) EDS spectrum for a Si-CNF without annealing, and (f) EDS spectrum corresponding to Fig. 5.3(b). Inset in (b): TEM image for a typical Si-CNF without annealing (different sample from the annealed SON).

The fiber shape and size (diameter and length) was almost identical before and after annealing [see also the inset in **Fig. 5.3(b)**]. **Fig. 5.3(b) and 5.3(c)** show low and high magnification TEM images of a tip region of the SON, respectively. As seen in **Fig. 5.3(c)**, the SON is amorphous in crystalline structure. This is confirmed also by an electron diffraction pattern (EDP) of the SON, disclosing weak hallow around the incident electron beam [**Fig. 5.3(d)**].

Before annealing, the fiber was Si-CNF. So the compositional analysis for both Si-CNF and SON is indispensable. **Fig. 5.3(e)** shows an energy dispersive x-ray spectroscopy (EDS) spectrum obtained for a Si-CNF without annealing, revealing that the fiber composed mainly of C and Si as expected. By contrast, annealed fiber is shown in **Fig. 5.3(b)** composed mainly of Si and O with very small amount of C, as confirmed by EDS [**Fig. 5.3(f)**]. From a simple quantification of EDS, composition of the formed SON was about Si: O: C = 38: 60: 2 (atomic %). (For the contained C, it was not clear whether it was due to the residual C of CNF or contamination.) Thus, it was confirmed that the fiber on the cantilever after annealing was surely SON with the amorphous structure.

5.3.2. X-TEM observation of ZnO films

Fig. 5.4(a) shows a low magnification TEM image which is corresponding to X-TEM image for a ZnO film deposited onto a SON tipped cantilever at room temperature followed by post-annealing at 400^{o}C in air. As seen also in **Fig. 5.4(b)**, which is a medium magnification TEM image of the tip region of the ZnO sample, the deposited ZnO film was clearly recognizable by a darker contrast of ZnO film than that of the SON. At a glance, the ZnO film was not columnar, but fine granular. (This point will be discussed later.) The thickness of the deposited ZnO was measured to be 22 nm. Although the thickness of the ZnO film deposited onto the "back" side of the SON was rather small (~7 nm), the ZnO film was deposited onto not only the "front" side of the SON facing to the ZnO source but also the "back" side of SON [see also **Fig. 5.2(b)**], because of the relatively high pressure, and hence the short mean free path of the film composing particles during the film deposition. **Fig. 5.4(c)** shows a high magnification TEM image of the ZnO film deposited onto the very tip of the front side of the SON [rectangular in **Fig. 4(b)**], revealing that the ZnO film was granular and polycrystalline composed of fine grains of about 15 nm. The polycrystalline nature of the ZnO film was proven also in the EDP

[**Fig. 5.4(d)**] taken at the region corresponding to **Fig. 5.4(b)**. **Fig. 5.4(e)** shows a high resolution TEM image of the arrow-indicated area in **Fig. 5.4(c)**, disclosing the well crystallized grains with the periodic lattice fringes (inter layer distance) of 0.247 nm which corresponds to ZnO (101) lattice plane.

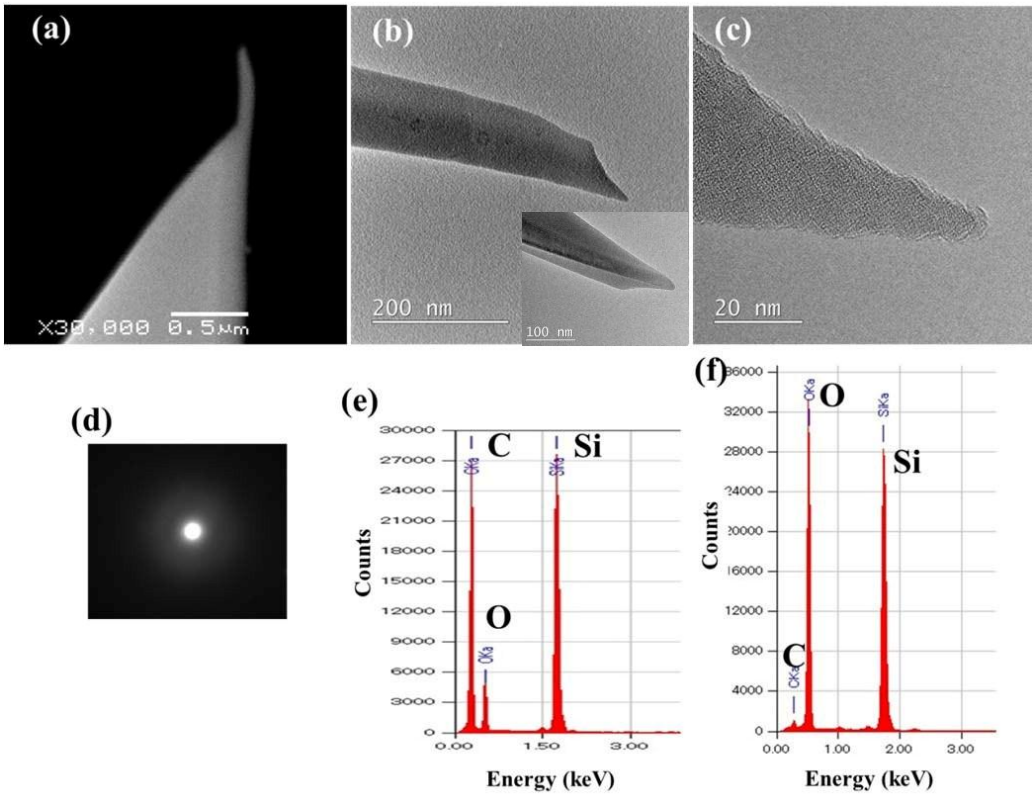

Figure 5.4: (a) Low and (b) medium magnification X-TEM images of a ZnO/SON sample annealed at 400^{o}C in air. (c) High magnification X-TEM image of the rectangular in Fig. 5.4(b). (d) EDP corresponding to Fig. 5.4(b). (e) High resolution X-TEM image of the arrow-indicated area in Fig. 5.4(c).

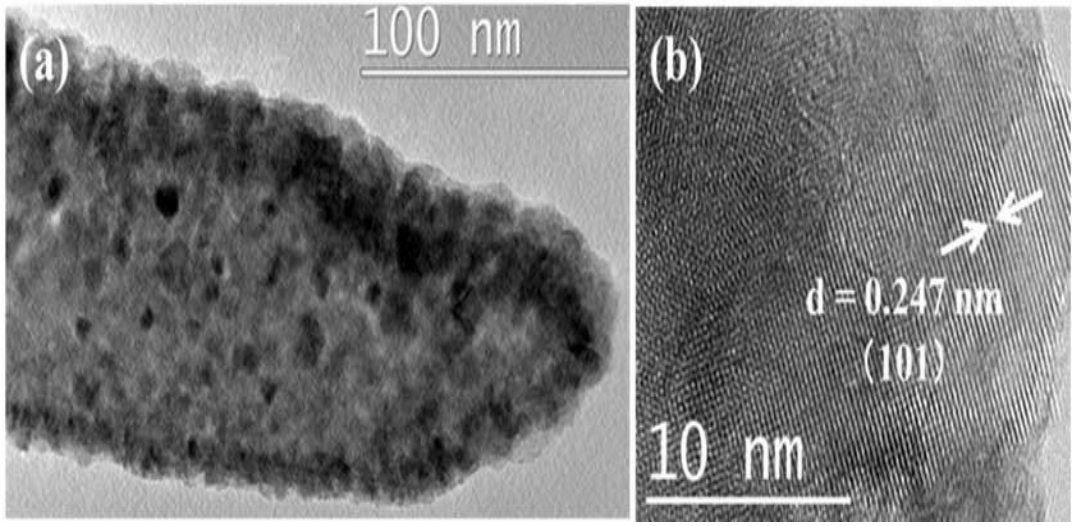

Figure 5.5: (a) X-TEM image of an as-deposited ZnO film (without annealing) onto a SON, and (b) high resolution X-TEM image of the tip region

In order to check the annealing effect of APD deposited ZnO films, TEM (X-TEM) observation of an as-deposited ZnO film (without annealing) onto SON was also carried out. **Fig. 5.5(a)** shows a TEM image of the tip region of a ZnO deposited SON, revealing that the ZnO consisted of the agglomeration of well-crystalized [**Fig. 5.5(b)**] but smaller grains (about 9 nm in average) than those after annealing (about 15 nm in average). For zincblende structured films, such as ZnO films, thin films sometimes show the (002) oriented (c-axis oriented) columnar structure [26]. However, it was not the case for the films deposited by APD method, as seen in **Figs. 5.4** and **5.5**. In order to check this point, ZnO film deposition was carried out also at 400^{o}C. However, the (002) oriented columnar structure was not prominent and the lattice image observed for respective grains was almost similar to that of **Fig. 5.4(e)**. The energy of the depositing particles is known to be relatively high for APD method [27]. This would be responsible for the relatively small grains and the diversity of crystal orientation. This would be the reason why APD method is applicable for the deposition of novel nanoparticles and films.

5.4. Conclusion

Based on the technique for the ion-induced CNF fabrication, Si-CNFs were fabricated onto AFM cantilever tips. The formed Si-CNFs were then annealed at 1000^{o}C in atmospheric ambient to form SON tipped cantilevers. The SON, linear in shape, was characterized to be amorphous in crystalline structure and almost silicon oxide in composition. ZnO films deposited by an APD method onto these SON tipped cantilevers at room temperature and at an elevated temperature (400^{o}C) were not c-axis (002) oriented columnar but were featured by the agglomeration of well crystalized fine grains, as revealed by the X-TEM observation. Thus, it is believed that the SON tipped cantilever is promising as a substrate for simple and rapid X-TEM analyses. The next step is the dynamic X-TEM observation of the graphene formation at the interface between the catalyst and the SiO_2 substrate at low graphitization temperatures using low melting point catalysts. This is my future subject.

5.5. References

[1] J. Ayache, L. Beaunier, J. Boumendil, G. Ehret and D. Laub, "Sample Preparation Handbook for Transmission Electron Microscopy: Techniques." 2010.

[2] V. B. Özdöl, V. Srot, and P. A. van Aken, "Sample preparation techniques for transmission electron microscopy" G. In and Van Tendeloo (Ed.) in "Handbook of Nanoscopy," pp. 473-498. Weinheim: Wiley-VCH Verlag GmbH & Co. KGaA, 2012.

[3] N. Bassim, K. Scott and L. A. Giannuzzi, MRS Bull. **39**, 317, 2014.

[4] M. Tanemura, T. Okita, H. Yamauchi, S. Tanemura and R. Morishima, Appl. Phys. Lett. **84**, 3831, 2004.

[5] M. Tanemura, H. Hatano, M. Kitazawa, J. Tanaka, T. Okita, S. P. Lau, H. Y. Yang, S. F. Yu, L. Huang, L. Miao, and S. Tanemura, Surface Science **600**, 3663, 2006.

[6] M. Tanemura, T. Okita, J. Tanaka, M. Kitazawa, K. Itoh, L. Miao, S. Tanemura, S. P. Lau, H. Yang, and L. Huang, IEEE Transactions on Nanotechnology **5**, 587, 2006.

[7] M. Tanemura and S. P. Lau: "Flexible Field Emitters: Carbon Nanofibers (Chapter 15.)" in "Carbon Nanotube and Related Field Emitters: Fundamentals and Applications" Edited by Y. Saitoh, Wiley-VCH Verlag GmbH & Co. KGaA (Weinheim) 2010.

[8] M. S. Rosmi, M. Z. Yusop, G. Kalita, Y. Yaakob, C. Takahashi and M. Tanemura,Sci. Rep. **4**, 7563, 2014.

[9] M. Z. M. Yusop, P. Ghosh, Y. Yaakob, G. Kalita, M. Sasase, Y. Hayashi, M.Tanemura, ACS Nano **6**, 9567, 2012.

[10] C. Takahashi, Y. Yaakob, M. Z. M. Yusop, G. Kalita, M. Tanemura, Carbon **75**, 277, 2014.

[11] Y. Yaakob, M. Z. M. Yusop, C. Takahashi, M. S. Rosmi, G. Kalita and M.Tanemura,

RSC Advance **5**, 5647, 2015.

[12] M. S. Rosmi, Y. Yaakob, M. Z. M. Yusop, S. Sharma, R. Vishwakarma, M. I. Araby, G. Kalita, and M. Tanemura, RSC Advances **6**, 82459, 2016.

[13] Y. Sugita, M. Kitazawa, M. Z. M. Yusop, M. Tanemura, Y. Hayashi and R. Ohta, Journal of Vacuum Science and Technology B **27**, 980, 2009.

[14] Z. Wang, M. Z. M. Yusop, T. Hihara, P. Ghosh, A. Hayashi, Y. Hayashi and M. Tanemura, Journal of Nanoscience and Nanotechnology **11**, 10677, 2011.

[15] Y. Yaakob, M. Z. Yusop, G. Kalita and M. Tanemura, Physica Status Solidi B **252**, 1345, 2015.

[16] Masaki Tanemura and Masashi Kitazawa: "Fabrication of Ion-Induced Carbon Nanocomposite Fibers and their Application to Magnetic Force Microscope Probes" in "Advances in Nanocomposites - Synthesis, Characterization, and Industrial Applications" Edited by Boreddy Reddy (InTech Publisher), Chapter 35, 2011.

[17] S. Sharma, M. S. Rosmi, Y. Yaakob, M. Z. M. Yusop, G. Kalita, M. Kitazawa and M. Tanemura, Carbon **132**, 165, 2018.

[17] M. Tanemura, M. Kitazawa, J. Tanaka, T. Okita, R. Ohta, L. Miao, and S. Tanemura, J. Appl. Phys. **45**, 2004, 2006.

[18] J. Tanaka, M. Kitazawa, M. Tanemura, and R. Ohta, Journal of Physics: Conference Series **61**, 1167, 2007.

[19] M. Kitazawa, R. Ohta, Y. a Sugita, K. Inaba, and M. Tanemura, Journal of Vacuum Science and Technology B **27**, 975, 2009.

[20] K. Inaba, K. Saida, P. Ghosh, K. Matsubara, M. Subramanian, A. Hayashi, Y. Hayashi,

M. Tanemura, M. Kitazawa, and R. Ohta, Carbon **49**, 4191, 2011.

[21] M. Kitazawa, S. Ito, A. Yagi, N. Sakai, Y. Uekusa, R. Ohta, K. Inaba, A. Hayashi, Y. Hayashi and M. Tanemura, Japanese Journal of Physics **50**, 08LB14 ,2011.

[22] S. Takahashi, H. Chiba, T. Kato, S. Endo, T. Hayashi, N. Todoroki and T. Wadayama, Phys. Chem. Chem. Phys. **17**, 18638, 2015.

[23] N. Todoroki, T. Kato, T. Hayashi, S. Takahashi, and T. Wadayama, ACS Catal. **5**, 2209, 2015.

[24] K. Hanada, T. Nishiyama, T. Yoshitake, and K. Nagayama, Diamond & Related Materials **19**, 899, 2010.

[25] Y. Fujita, K. Moriyama, Y. Hiragino, Y. Furubayashi, H. Hashimoto, and T. Yoshida, Phys. Status Solidi C **11**, 1260 ,2014.

[26] F. C. M. van de Pol, F. R. Blom, and Th. J. A. Popma, Thin Solid Films **204**, 349, 1991.

[27] A. Anders and E. Oks, J. Appl. Phys. **101**, 043304, 2007.

Chapter 6. Conclusions

6.1. Overall Conclusions

Most of the reported graphene synthesis include the high-temperature process. Nevertheless, low-temperature growth should be achieved for a wider range of practical applications. Thus, much effort has been devoted to reducing the growth temperature, and this subject is still challenging.

Deep thinking on the role of a catalyst Cu in CVD process led me to an important consequence, namely, the melting point of a catalyst must play an important role in the low-temperature graphene growth. Based on this thinking, two strategies were attempted for the selection of the catalyst to achieve the low-temperature graphene growth; one is the selection of the catalyst material itself and another is the nano-sized catalyst to lower the melting point of the metal.

On the selection of the catalyst material itself, In whose melting point is 156.6^{o}C was employed as the catalyst. In order to observe the local graphitization by TEM, In-included In-CNFs were fabricated on an edge of a carbon foil by Ar^{+} ion sputtering of both the carbon foil and an In plate. Depending on the ion energy, graphitization catalyzed by In was observed even for the as-sputtered sample without post-annealing, suggesting that In is promising as the catalyst for the low-temperature graphene growth. Encouraged by this fact, a stacked film of In and amorphous C was deposited onto a SiO_2 covered Si substrate, and this thin film sample was then annealed in vacuum at 150 and 200^{o}C. In both cases, a clear 2D peak in Raman spectra, which is the evidence of the graphene formation, was observed. Thus, the low melting point metal was concluded to be a key for the low-temperature graphene formation. This finding will open up the synthesis of graphene at further lower temperatures.

On the effect of the catalyst size, Sn nanoparticles 2-4 nm in size dispersed in the amorphous C matrix (CNF) was investigated. TEM observation demonstrated that the local graphitization started to occur at the temperature as low as 180^{o}C due to the decrease in the melting point for nanoparticles. The combination of low melting point metal and its nanoparticle form would be the new strategy for the lower temperature graphene growth.

For the future X-TEM observation of catalyst/graphene/substrate interface, the fabrication of SON as a model substrate requiring no post-treatment for X-TEM was also challenged based on the fabrication of the Si included CNFs (Si-CNFs) on AFM cantilever tips. The formed Si-CNFs were then annealed at 1000^{o}C in atmospheric ambient to form SON tipped cantilevers. The SON, linear in shape, was characterized to be amorphous in crystalline structure and almost silicon oxide in composition. In order to check the performance of this SON, ZnO films deposited thereon were analyzed by X-TEM, revealing the agglomeration of well crystalized fine ZnO grains with clear lattice images. Thus, it is believed that the SON is promising as the platform for the X-TEM analyses.

6.2. Future Prospect of the work

My next step is to find a suitable alloy for lower temperature graphene synthesis. So, I will study a different combination of metals and their catalytic property to synthesis graphene near room temperature. By lowering the graphene synthesis temperature, I will try to fabricate graphene on plastic which can have practical applications such as interconnection. For this aim, the alloy catalysts and carbon films will be deposited onto SiO_2 substrates. After the graphene film growth, surface morphologies, thickness, graphene quality, and crystalline structure will be examined by field emission scanning electron microscopy, atomic force microscope, Raman spectroscopy, and atomic resolution TEM, respectively. Also, I will observe the catalytic

behavior of low melting point metals and nano-sized catalysts in the atomic dimension by X-TEM using this SON as the substrate.

List of publications

1) ***Mona Ibrahim Araby,*** Mohamad Saufi Rosmi, Riteshkumar Vishwakarma ,Subash Sharma - Yuji Wakamatsu - Kazunari Takahashi - Golap Kalita - Masashi Kitazawa - Masaki Tanemura; Graphene formation at 150 °C using indium as catalyst; RSC Adv., 7 (2017) 47353-47356.

2) Kouki Watanabe, Subash Sharma, ***Mona Ibrahim Araby***, Masahide Shima, Takumi Harada, Mohamad Saufi Rosmi, Golap Kalita, Masashi Kitazawa and Masaki Tanemura; Development of oxide nanofiber tipped cantilever as a substrate for cross sectional transmission electron microscopy analysis; Surf Interface Anal. 50 (2018) 1122-1126.

3) ***Mona Ibrahim Araby***, Subash Sharma, Sahar Elnobi, Golap Kalita, Masashi Kitazawa and Masaki Tanemura; Temperature dependence of catalytic activity in graphene synthesis for Sn nanoparticles; Journal of Materials Science: Materials in Electronics (JMSE), (2019).

4) Mohamad Saufi Rosmi, Yazid Yaakob, Mohd Zamri Mohd Yusof, Subash Sharma, Ritesh Vishwakarma, ***Mona Ibrahim Araby***, Golap Kalita, and Masaki Tanemura; In situ fabrication of graphene from a copper–carbon nanoneedle and its electrical properties; RSC Adv. 6 (2016) 82459-82466.

5) Riteshkumar Vishwakarma, Mohamad Saufi Rosmi, Kazunari Takahashi, Yuji Wakamatsu, Yazid Yaakob, ***Mona Ibrahim Araby***, Golap Kalita, Masashi Kitazawa,

Masaki Tanemura; Transfer free graphene growth on SiO_2substrate at 250 °C; Scientific Reports, 7 (2017) 43756.

6) Subash Sharma, Kamal Sharma, Mohamad Saufi Rosmi, Yazid Yaakob, ***Mona Ibrahim Araby***, Hajime Ohtani, Golap Kalita, Masaki Tanemura; Morphology-Controlled Synthesis of Hexagonal Boron Nitride Crystals by Chemical Vapor Deposition; Crystal Growth & Design, 16, (2016) 6440-6445.

7) Subash Sharma, Balaram Paudel Jaisi, Kamal Prasad Sharma, ***Mona Ibrahim Araby***, Golap Kalita, Masaki Tanemura; physica status solidi, Synthesis of Freestanding WS_2 Trees and Fibers on Au by Chemical Vapor Deposition (CVD); physical status solidi A 215(2018) 1700566.

List of conference

1) **Mona Ibrahim Araby**, Mohamad Saufi Rosmi, Riteshkumar Vishwakarma, Subash Sharma, Golap Kalita and Masaki Tanemura.; In Situ Transmission Electron Microscopy Observation of Graphitic Carbon Layer Formation for Sn-included Carbon Nanofiber During Current Flow .; The 8th International Symposium on Surface Science conference,.22 - 26 October 2017 , Tsukuba International Congress Center, Tsukuba Japan.

2) **Mona Ibrahim Araby**, Subash Sharma, Golap Kalita and Masaki Tanemura.; TEM Observation of Graphitization at 250^{o}C for Amorphous Carbon Nanofibers Including Novel Catalyst Nanoparticles.; The 30th International Microprocesses and Nanotechnology Conference November 6 - 9, 2017, Ramada Plaza JeJu Hotel, JeJu, Korea.

3) **Mona Ibrahim Araby** , Subash Sharma , Mohamad Saufi Rosmi , Golap Kalita and Masaki Tanemura .; Towards the graphene formation at 150 ^{o} C .;The 65thJSAP Spring Meeting, 2018.; 17– 20, 2018, VenueWASEDA University, Nishiwaseda Campus and bell salle Takadanobaba, Japan.

4) Subash Sharma, **Mona Ibrahim Araby,** Golap kalita and masaki Tanemura. Joul heat induced synthesis of Y junction carbon nanotube in in-situ TEM. The 65th JSAP Spring Meeting, 2018. 17– 20, 2018, VenueWASEDA University, Nishiwaseda Campus and bell salle Takadanobaba, Japan.

5) **Mona Ibrahim Araby**, Subash Sharma, Sahar Elnobi, Golap Kalita, and Masaki Tanemura. Temperature dependence of catalytic activity in graphitization for Sn nanoparticles. 31st International Microprocesses and Nanotechnology Conference November 13-16, 2018, Sapporo Park Hotel, Sapporo, Japan.